Preprints (www.preprints.org) | NOT PEER-REVIEWED | Posted: 8 October 2019 doi:10.20944/preprints201910.0079.v1

*Article*

# Sol Hamed ophiolitic complex, southern Eastern Desert, Egypt: Petrological, economic potentiality and structural implications

**Tarek Sedki [1,] *, Shehata Ali [1] , Haroun A. Mohamed [1] and Rafat Zaki [1]**

[1] Geology Department, Faculty of Science, Minia University, El–Minia, 61519, Egypt

* Correspondence: t.sedki@yahoo.com; Tel.: (+201101155505)

**Abstract**:

The Sol Hamed (SH) area is a part of the Arabian-Nubian Shield (ANS) ophiolites occurred within Onib-Sol Hamed suture zone in the southern Eastern Desert of Egypt. The ophiolitic assemblages in this area are represented by serpentinite, metagabbro and arc assemblages represented by metavolcanics. They later intruded by gabbroes and granites.

Geochemically, the compatible trace elements (Cr=2426–2709 ppm, Ni=1657–2377 ppm and Co=117–167 ppm) enrichment in SH serpentinites indicate derivation from a depleted mantle peridotite source. They show affinity to the typical metamorphic peridotites. The normative compositions reflect harzburgitic mantle source. Their $Al_2O_3$ contents (0.05–1.02 wt. %) are akin to oceanic and active margin peridotites and Pan-African serpentinites. The Cr and $TiO_2$ contents indicate supra-subduction zone (SSZ) environment. Their $Al_2O_3/SiO_2$ and $MgO/SiO_2$ ratios support the SSZ affinity and are similar to ANS peridotites with fore-arc setting. Moreover, their $Al_2O_3$ and CaO depletion is typical of fore-arc peridotites.

Structurally, the area represents four deformational events can be well-known in the Neoproterozoic rocks ($D_1$, $D_2$, $D_3$ and $D_4$); $D_1$: E–W thrust faults and related E–W ($F_1$) folds; $D_2$: NW–SE thrust faults and related NW–SE ($F_2$) folds were formed; $D_3$: conjugate NNW-trending sinistral and NNE-trending dextral transpression, as well as N–trending tight folds ($F_3$) and $D_4$: is E–W dextral strike-slip and dip-slip normal faults striking NNW–SSE to N–S and E–W may be related to Red Sea rifting. There are major three fault sets affected the area. The first set trend mainly NE-SW and is manifested in the volcanic-sedimentary assemblage and Gabal SH and have important role in mineralization. The second set trend E-W affecting all the basement rocks and disturbs the first fault set. The third set trend N-S affected all the rock units.

Magnesite mineralization in SH serpentinites is cryptocrystalline formed due to hydrothermal alteration of the serpentinite host rocks. It is occur as snow-white veins and stock-works. These characteristics are typical of Kraubath type magnesite deposits.

Gold mineralization is confined to malachite-bearing quartz veins, smoky quartz veins and alteration zones. Malachite-bearing quartz veins trending NW-SE cut through gabbroic rocks and exhibit mylonitic structure. They are fractured containing malachite and disseminated sulfide minerals. Smoky quartz veins trending NE-SW with SE steeply dipping intrude the meta-andesite. They are intensively sheared containing iron oxides in the fissures. The gold grades increase with arsenopyrite occurrences. On the other hand, the barren quartz veins are nearly vertical with E-W directions. Alteration zones with NW-SE trend and nearly vertical dip intrude metagabbros and metavolcanics. Hematite, limonite, goethite and fresh pyrite characterize these zones. They occur mainly neighboring the auriferous quartz veins.

**Keywords:** Sol Hamed; Supra-subduction zone; Serpentinites; Magnesite mineralization; Gold deposits.

## 1. Introduction

The Arabian–Nubian Shield (ANS) crustal growth occurred during the Neoproterozoic Era [1]. The ANS represents a combination of well-preserved tectono-stratigraphic terrains characterized by well-defined suture zones which are marked by ophiolite assemblages [2-4]. During mid-Neoproterozoic, Juvenile arc terrains formation around Mozambique Ocean margins and collision occurred producing the ANS [3, 5, 6]. In late Neoproterozoic (~630 Ma), arc accretion terminated once East and West Gondwana fragments collision occurred closing the Mozambique Ocean and generating the East African–Antarctic Orogen [7, 8]. Therefore, ANS suture zones are classified to older arc–arc suture zones which separated ~700–870 Ma arc terrains and younger arc–continent suture zones formed at ~630 Ma [2, 9-12]. It is generally accepted that most of the ANS ophiolites

Preprints (www.preprints.org) | NOT PEER-REVIEWED | Posted: 8 October 2019 doi:10.20944/preprints201910.0079.v1



were generated in supra-subduction zone (SSZ) environment [13-18]. They formed due to seafloor spreading above active subduction zones. Several tectonic scenarios were attributed for the ANS ophiolites formation: (1) NMORB setting (i.e., fragments of normal oceanic crust;[19] (2) remnants of back-arc basins (e.g., [9, 20, 21]); or (3) fore-arc setting due to seafloor spreading during initiation of subduction process [4, 13-15, 17, 22] . Various ophiolite complexes may possibly generated in diverse SSZ tectonic settings. In order to contribute to resolve this existed debate, we introduce new geochemical data on Sol Hamed serpentinites in the southern Eastern Desert to better constraint their tectonic setting. The Egyptian Precambrian belt which is the NE part of the ANS is consisted of an Upper Proterozoic assemblages of volcano-sedimentary succession, scattered over thrusting mafic-ultramafic rocks (i.e., ophiolite complex) and intruded by syn- to late-tectonic granitoids and mafic–ultramafic intrusions. Later, Precambrian peralkaline granites and Tertiary alkaline ring complex intrude the country rocks of the area. The Sol Hamed ophiolitic complex is a part of Allaqi-Heiani-Onib-Sol Hamed-Yanbu arc-arc suture (Fig. 1; [23, 24] which represent one of the two longest and most complete Neoproterozoic ophiolite suture in the Arabian Nubian Shield [25].

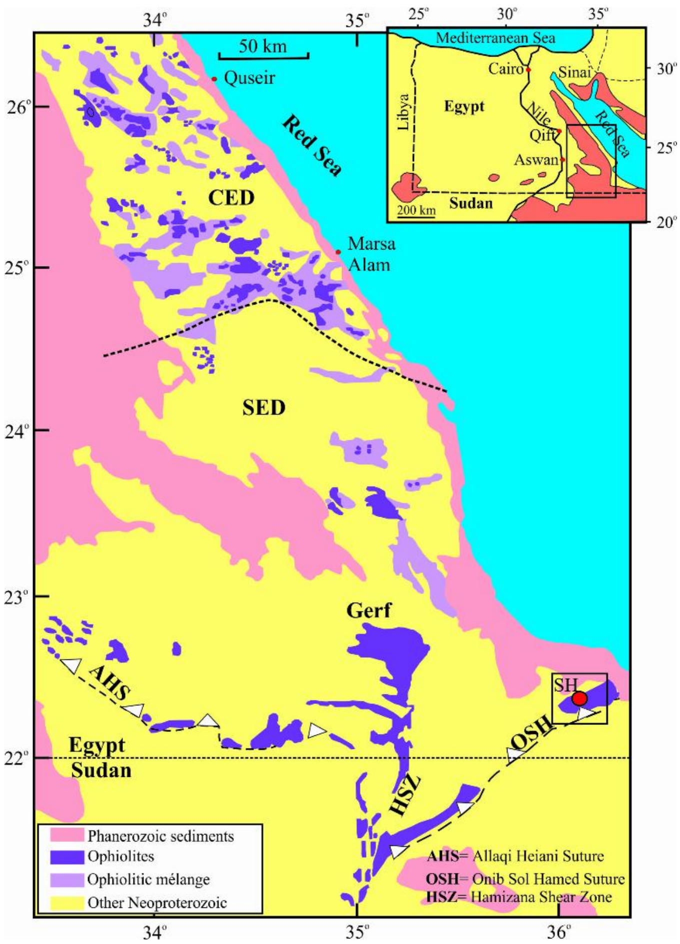

 doi:10.20944/preprints201910.0079.v1



**Figure 1**. Map showing the distribution of ophiolites in the central Eastern Desert (CED) and southern Eastern Desert (SED) of Egypt (Modified from [24]). The location of Sol Hamed (SH) ophiolites is also indicated. The inset map shows the general map of Egypt.

## 2. Materials and Methods

**The work includes both field and laboratory works.**

### 2.1. Field study

For this purpose, field trip was carried out during the period of (20-27) April 2019 by using the landsat image and the available geologic maps (scale 1:50000) were used. About 15 rock samples were collected representing the exposed serpentinites in the mapped area (Fig. 2). Thin sections were prepared for each sample.

### 2.2. Laboratory work

For this purpose, petrographic investigation of about 15 thin sections and 4 polished sections were prepared. The petrographical study was achieved using MEIJI ML 9000 Polarizing Microscope equiped with automatic photo micrographic attachement ToupCam Digital Camera XCAM1080PHA. Chemical analyses of 10 samples were carried out at the Central Laboratories of the Geological Survey of Egypt. The selected samples represent the best aerial coverage of the examined area. Before bulk rock chemical analyses were carried out, the samples were cleaned and grinded in an electric agate mill, homogenized, dried on the oven for 60 min at 105 degree then mix with 50% from wax polyvinyl meta-acylate additives. Determination of the chemical composition of both major and some trace elements was performed by using a Philips x-ray fluorescene technique model PW/2404, with Rh radiation tube and eight analysing crystals. Crystal (LIF-200) was used for estimating Ca, Fe, K, Ti and Mn, while crystal (TIAP, PX-1) was used for estimating Mg and Na. Crystal (Ge) was used for estimating P and Crystal (PET) was used for estimating Si and Al. The concentration of the analysed elements was determined by using software Super-Q with accuracy 99.5 % and confidence limite 95.6 %. Ten samples of these rocks were also analysed to determine their REE contents using the simultaneous inductively coupled plasma emission spectrometer (720 ICP-OES, Agilent Technologies), with accuracy 96 %. Nine samples from SH

Preprints (www.preprints.org) | NOT PEER-REVIEWED | Posted: 8 October 2019 doi:10.20944/preprints201910.0079.v1



magnesites were analyzed for major elements by the same technique of XRF mentioned above. All analytical results are given in Table 1 and 2.

**3. Geologic setting**

Sol Hamed area located in north of Gabal Elba in the southern Eastern Desert. Its rock units consist of mainly ophiolitic assemblage and arc-related metavolcanics and granitoids.

Ophiolite complex contains three NE-SW trending sub-vertical lithological zones, ultramafic in the NW side, gabbroes in the middle and pillow lava in SE (Fig. 2). This belt signifies the north-eastern outlet of the Hamizana Shear Zone (Fig. 1). The ophiolitic ultramafics include both sheared and massive verities. Serpentinites show low to medium relief. They cropped out in the central and eastern parts. Furthermore, they are transformed along NE-SW trending shear zones to talc, talc- and quartz-carbonates, and magnesite particularly in the eastern parts. Most quartz carbonates present in the area sideways the contact between serpentinites and metavolcanics. Magnesites fill the cracks and fissures creating stock-work within the serpentinite (Fig. 3a).

The massive ultramafic complex comprise serpentinized dunite, peridotite and pyroxenite. The serpentinized dunite swarm few chromite pods [26]. The complex is net-veined with white-blue grey magnesite filling the fractures due to hydrothermal alteration. Serpentinite is geologically bounded in NW and SE by schistose basic to intermediate metavolcanics and ophiolitic metagabbro, correspondingly.

Metagabbros befall as large masses of low to medium relief. They are serene in the southern part of the study area, separated by basic dykes (Fig. 3b) and quartz veins. They current SE of the serpentinites with a perfect tectonic contact trending NE–SW and dip to NW (Fig. 2). They are locally layered, sheared and warped as flaser structure (Fig. 3d). They are cut by acidic dykes of apogranite (Fig. 3e) and metagabbro-diorite dykes forming parallel and nearly vertical NE-SW trending dykes (Fig. 3b). They are also intruded by post-tectonic granitoids (i.e., tonalite and monzogranite) at SE of Gabal Sol Hamed (Fig.3f).

Basaltic pillow lavas situated NW to W of Gabal Qash Amer and related with the volcaniclastics. The original pillow customs are easily familiar and dip to the SW. They have go through constrain deformation designated by the lineated and stretched pillow volcanics.

Preprints (www.preprints.org) | NOT PEER-REVIEWED | Posted: 8 October 2019 doi:10.20944/preprints201910.0079.v1



The arc assemblages comprise basic to intermediate metavolcanics and their pyroclastics. The acidic metavolcanics display schistose structure with main direction of 50o and dip 60o SE. The meta-rhyolites showing at the northeastern and western part of the area, wounding by quartz veins and enclosed by sand dune particularly in the north central part. The massive basic to intermediate metavolcanics produce out at the northern part. In the western side of Wadi Diit a small belt of massive and schistose metavolcanics is observed (Fig. 2). These rocks are slightly foliated and comprise thin beds of fine laminated volcaniclastics and tuffs. There are also lapilli tuffs with plagioclase and quartz clasts of lapilli size. Gradational connection with gabbroic rocks existing south of the volcanic rocks. North of this volcanic belt, there is a sharp intrusive contact with tonalite rocks.

The arc granitoids with low to medium relief crop out at the NW part of the area and are characterized by presence of dioritic xenoliths.

Granitic rocks befall in Qash Amer and El Sela area. Qash Amer muscovite granites signify the highest peak in the area. They are categorized by fractures, exfoliation, and weathering boulders. The El Sela younger granites take place as high-relief remote and dispersed granitic masses vacating the southern East part of the mapped area (Fig. 2). They are characterized by cavernous weathering and exfoliation. They interrupt younger metavolcanics and are occupied by different types of trachytic dikes and quartz. These granites show joints and fractures that are occupied by iron oxide containing radioactive minerals (Ali, 2013; Abouelnaga et al., 2014).

Numerous basic and acidic dykes separated the area. Acidic dykes are detailed in Wadi Diit, where they cut tonalite and metavolcanics. Generally, they are trending either NE-SW or N-S. They include rhyolite, apogranite and dacite. Basic dykes are abundant and trend mainly either NE-SW or NW-SE. They changed through all the rock units described above particularly tonalite, metavolcanics and ophiolitic gabbro (Fig. 3b). They comprise andesite and dolerite (Fig. 3b) with N-S trend.

The veins can be subdivided into three main types, quartz, and ankerite and pegmatite veins. The studied area is rich in quartz veins with different thickness trending mainly N-S and NE-SW particularly in the metavolcanics. It is white color and sometimes rich with iron oxides and copper minerals. Other types of quartz are brecciated, cemented by iron oxides (Fig. 3c). Sometimes, smoky quartz detailed especially in the gabbroic rocks. Quartz veins cut through all the rock units. The veins are brecciated, stained red with iron oxides and may comprise pyrite crystals (Fig. 3c). Many

Preprints (www.preprints.org) | NOT PEER-REVIEWED | Posted: 8 October 2019 doi:10.20944/preprints201910.0079.v1



quartz veins are supplementary with hydrothermal alteration zones in the metavolcanic rocks. Ankerite veins befall as big veins at junction of Wadi Diit with Wadi Badbari. They changed the schistose metavolcanics, trending either NE-SW or E-W with a vertical dip.

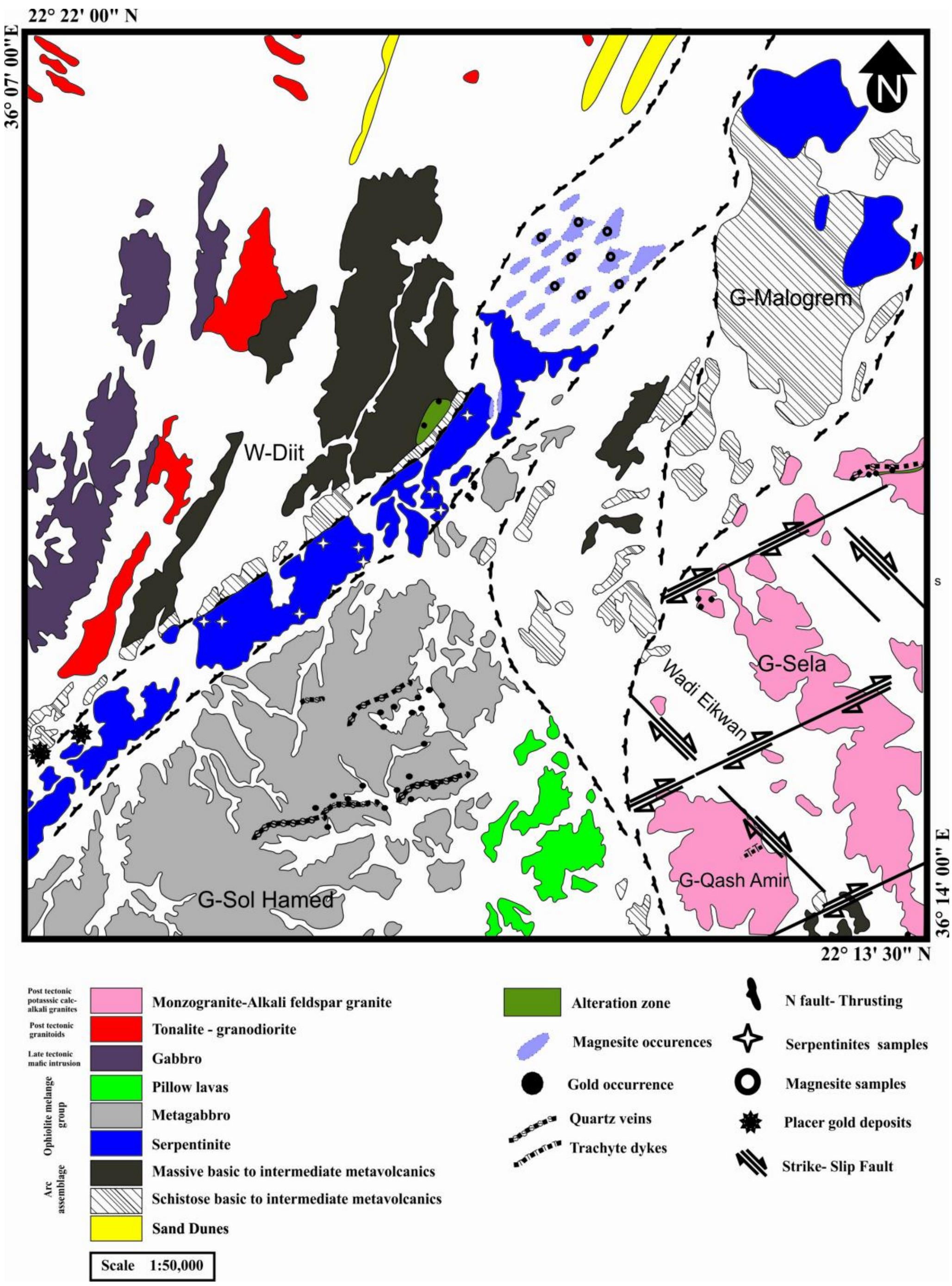


**Figure 2**. Geological map of SH (after EMRA, 1995, [77]).


**Figure 3.** Field photographs show a) the stock-work in magnesite bearing serpentinites, b) Bas basic dyke cutting the ophiolitic gabbro, c) Brecciated quartz-vein, d) Flaser structure of metagabbro, e) acidic dykes of apogranite and f) post-tectonic granitoids intruded within metagabbro.

## 4. Petrography

### 4.1. Serpentinites

Preprints (www.preprints.org) | NOT PEER-REVIEWED | Posted: 8 October 2019 doi:10.20944/preprints201910.0079.v1



Serpentinites recorded in SH. They are fine-grained and light green to dark green in color and essentially consist of serpentine minerals (>80%) together with variable amounts of carbonates, magnetite (Fig. 4a), and brucite as well as chromian spinel. In few samples, talc is observed and Olivine is completely altered to serpentine and opaques along its irregular fractures. Clinopyroxenes are partially and/or completely altered to tremolite and chlorite. The rocks exhibit pseudomorphic (Fig. 4b) and interpenetrating textures. Antigorite is the main serpentine mineral together with lesser chrysotile and lizardite Antigorite occurs as large plates and fibrous and scaly aggregates (Fig. 4b). Chrysotile occurs as fibrous veinlets that commonly transformed into carbonate and traversing the antigorite matrix (Fig. 4a). In some parts, bastite texture is associated with schiller structure where magnetite define cleavage planes of the original orthopyroxene (Fig.4a). Chromian spinel in the serpentinites occurs as both subhedral to euhedral crystals (Fig. 4a) and irregular grains, while in the sheared varieties spinel is mostly brecciated. Carbonates occur as sparse crystals, patches, and fine aggregates.

### 4.2. Carbonate serpentinite

Carbonate serpentinites are composed of serpentine minerals and carbonates as the main components. Carbonates occur as an alteration product of serpentine minerals (Fig.4b) whereas; opaques represent the main accessories. Carbonate samples are mostly stained with iron oxides, whereas some appear as veinlets corroding rock.

### 4.3. Tremolite-talc rocks

Tremolite-talc rocks are composed of tremolite and talc together with olivine and orthopyroxene relics (Fig. 4c). Accessory minerals are represented by carbonates and opaques. Talc and tremolite are formed as alteration products of olivine and orthopyroxene. Tremolite forms fibro-lamellar sheaves piercing talc, orthopyroxene and olivine.

### 4.4. Ophiolitic Metagabbros

These metagabbros are massive, holocrystalline, medium to fine-grained with a greyish-green to dark green color. They show ophitic to sub-ophitic textures, and mainly consists of plagioclase (60-50%) and amphibole (40-30%), together with rare fresh relics of clinopyroxene. The secondary minerals are chlorite, zoisite, clinozoisite, epidote, sericite and calcite, while the accessories are sphene, apatite and opaque minerals.

Preprints (www.preprints.org) | NOT PEER-REVIEWED | Posted: 8 October 2019 doi:10.20944/preprints201910.0079.v1



Plagioclase crystals are euhedral to subhedral and many exhibit albite twinning. Variable alteration of plagioclase to epidote, zoisite and clinozoisite, as well as sericite, is observed. Zoning of plagioclase occurs, but is generally uncommon. Primary magmatic hornblende is less abundant and when observed it occurs as prismatic and bladed aggregates that poikilitically encloses fine crystals of plagioclase (Fig. 4d) and is variably altered to tremolite, actinolite and chlorite. The secondary amphibole are highly abundant and mainly represented by actinolite commonly pale green and moderately pleochroic, often simply twinned and occurs as fibrous prisms and tablets (Fig. 4d). Augite occurs as irregular shreds and remnants within the pseudomorphic amphibole (Fig. 4d). Chlorite is present as flakey and fibrous aggregates and is closely associated with amphibole, epidote and calcite. Epidote occurs as anhedral granular aggregates replacing plagioclase and amphibole. Accessory minerals such as apatite occurs as fine laths embedded in plagioclase and amphibole.

**4.5. The metavolcanoclastic rocks (meta-tuffs)**

The metatuffs are encountered in the western part of the mapped area but with restricted extension. They are massive, fine-grained, bedded, laminated and sometimes associated with thin bands of brownish opaque minerals. Microscopically, they are composed essentially of metamorphosed ash and lapilli tuffs, containing mineral and rock fragments. The mineral fragments are represented by plagioclase and quartz, whereas the rock fragments are andestic and rarely basaltic in composition (Fig. 4e).

**4.6. Metagabbro-diorite**

Microscopically, these rocks consist mainly of plagioclase, amphibole together with subordinate amounts of pyroxene and opaques. Few samples contain very small amounts of quartz. Opaques, sphene and apatite are the accessories, while calcite, actinolite, chlorite and epidote represent the secondary products. Ophitic and sub-ophitic textures are common, whereas the porphyritic texture is rarely observed. Plagioclase ranges in composition from labradorite to oligoclase and generally occurs as subhedral to anhedral crystals, partly saussuritized. Amphiboles are represented by less abundant primary, prismatic crystals of brownish green color and poiklitically enclosing minute crystals of plagioclase (Fig. 4f). Secondary hornblende is predominating and form pesudomorphs after pyroxene. It commonly occurs as pale green subhedral crystals sometimes enclosing small

Preprints (www.preprints.org) | NOT PEER-REVIEWED | Posted: 8 October 2019 doi:10.20944/preprints201910.0079.v1



crystals of plagioclase. Pyroxene occurs as relics of altered greenish blue crystals. It is commonly an augite altered to secondary hornblende as indicated by the presence of the original pyroxene in the core mantled by secondary hornblende (Fig. 4f).

**4.7. Diorite**

Mineralogically the diorites are composed mainly of plagioclase and hornblende (Fig. 4g). Locally, chlorite partially replaces hornblende and quartz is a minor constituent. Hypidiomorphic texture is characteristic, Apatite, zircon and Fe oxides are common accessories.

**4.8. Syn-tectonic granite**

These rocks are represented by micro-granite. It is medium-grained and shows granular to granular porphyritic in texture. It is made up of plagioclase, K-feldspars, quartz, muscovite, biotite (Fig. 4h), accessory minerals (zircon, opaque minerals), and secondary minerals (chlorite, sericite and calcite). Plagioclase constitutes about 40% of the granite. Crystals are anhedral and equant, and albite twinning is ubiquitous. Plagioclase crystals are usually un-zoned. Potassium feldspar constitutes up to 20% of the rock. It occurs as small irregular crystals, often totally or partially enclosed by plagioclase; in some instances, plagioclase with myrmekitic intergrowths appears to invade the adjacent orthoclase. Quartz constitutes about 30% or the granite. It occurs as medium-sized, anhedral crystals, sometimes with sutured margins, and also as small, drop-like inclusions in either feldspar. It generally has undulose extinction. Muscovite constitutes up to 10% of the rock. It occurs as euhedral isolated laths, sometimes with small rounded quartz inclusions, and sometimes occurs as ragged intergrowths with quartz. Occasional ragged crystals of biotite occur, which may be partially replaced by chlorite. Calcite occurs as fine interlocked crystals commonly form micro-bands or filling the polygonal spaces among the plagioclase laths.

 doi:10.20944/preprints201910.0079.v1



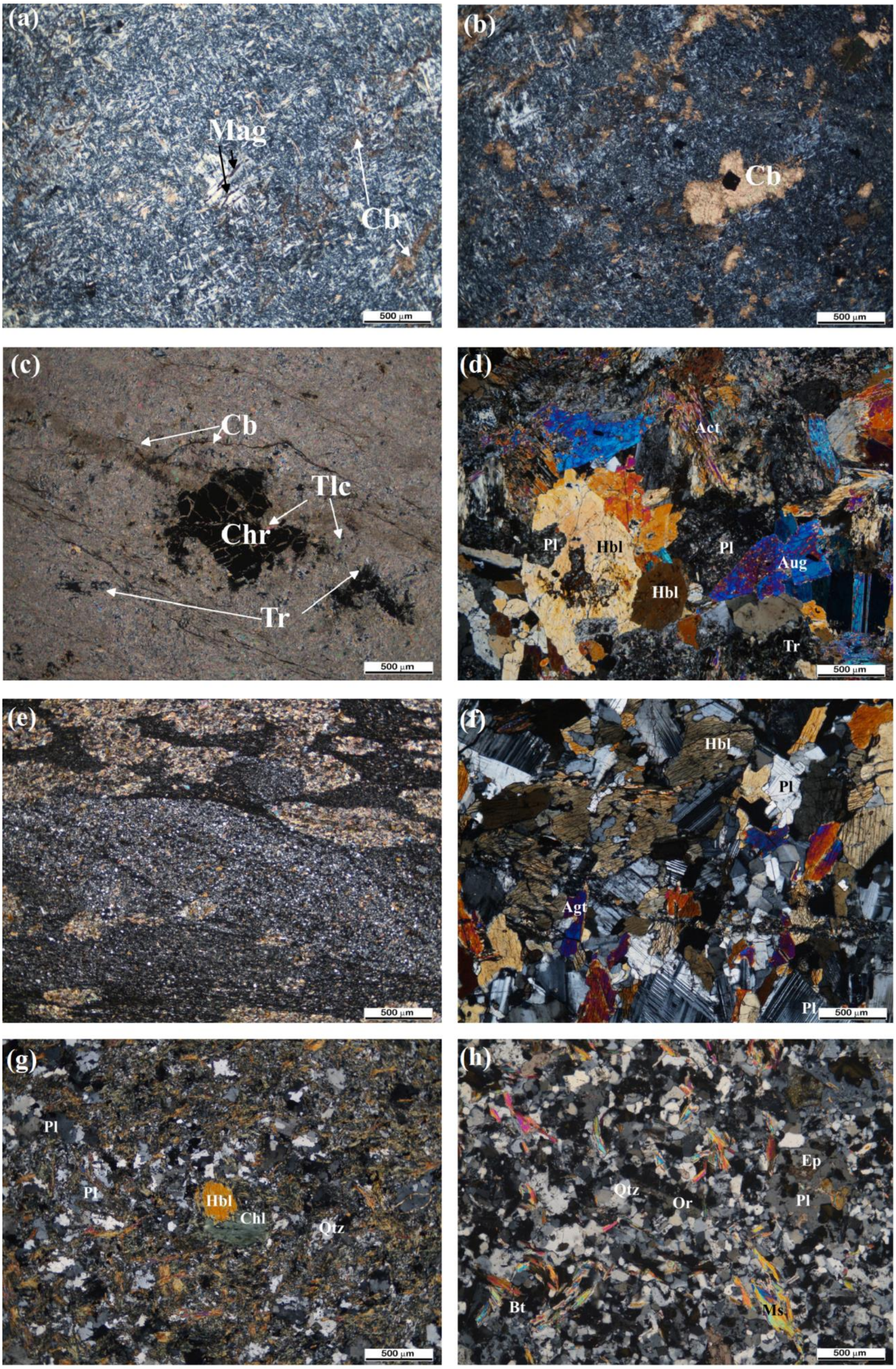


**Figure 4.** Photomicrograph showing a) Serpentinites with fine-grained and light green to dark green in color and consist of serpentine minerals organized with variable amounts of carbonates, magnetite, b) Pseudomorphic

Preprints (www.preprints.org) | NOT PEER-REVIEWED | Posted: 8 October 2019 doi:10.20944/preprints201910.0079.v1



and interpenetrating textures of serpentinites, carbonates as an alteration product of serpentine minerals, c) Tremolite-talc rocks composed of tremolite and talc together with olivine and orthopyroxene relics, d) Metagabbro with fine crystals of plagioclase and is variably altered to tremolite, actinolite and chlorite. The secondary amphibole are highly abundant and mainly represented by actinolite commonly pale green and moderately pleochroic, often simply twinned and occurs as fibrous prisms and tablets. Augite occurs as irregular shreds and remnants within the pseudomorphic amphibole, e) Andestic and basaltic composition of metatuffs, f) Crystals of plagioclase and Hornblende in metagabbro-diorite, g) Plagioclase and Hornblende in diorite and h) Plagioclase, K-feldspars, quartz, muscovite, biotite in syn-tectonic granite

## 5. Results

Major oxides recalculated on an anhydrous basis and plotted volatile-free to reduce the variable element dilution effects resulting from serpentinization process. The studied serpentinites have relatively higher loss of ignition (LOI) values (10.34–13.92 wt. %). The MgO content is hardly affected by serpentinization process and its elevated values in SH serpentinites (MgO=43.83–45.71 wt. %) reflect highly depleted mantle source [27, 28] . Their high Mg# (89.94–92.85) are like modern oceanic peridotites [29] indicating a limited mobility of Mg and Fe. Their very low $Na_2O$ (0.00–0.28 wt. %) and $K_2O$ (0.00–0.06 wt. %) contents are comparable to those from the Eastern Desert supporting this study [13, 15] . The serpentinization processes possibly increased the LOI contents without significant modification of the major element composition [30]. The Ca–metasomatism is a common issue in Egyptian serpentinites [31], however the very low CaO contents (0.05–0.75 wt.%) in the serpentinites indicates restricted effect of carbonate metasomatism. So, we suggest that the protolith major element compositions must have been preserved during the hydration processes and that the geochemistry of the studied serpentinites display mostly the original nature.

SH serpentinites display affinity to the typical metamorphic peridotites on the AFM diagram [32]; Fig. 5a. The bulk-rock $Al_2O_3$ content is relatively unaffected by serpentinization and therefore retains its original primary signature [29]. The studied serpentinites have $Al_2O_3$ contents (0.05–1.02 wt. %) comparable to oceanic and active margin peridotites and fore-arc and Pan-African serpentinites Fig. 5b; [13, 15, 18, 33, 34]. Like other Eastern Desert ultramafites, the SH serpentinites

Preprints (www.preprints.org) | NOT PEER-REVIEWED | Posted: 8 October 2019 doi:10.20944/preprints201910.0079.v1



have $SiO_2$/MgO ratios and $Al_2O_3$ contents analogous to ophiolitic peridotite [13, 15, 17, 19, 35, 36] Fig. 5c. The serpentinites the nature of peridotitic komatiite by using of Jensen's cation plot after [37], Fig. 5d. The $Al_2O_3$ and CaO depletion is typical of fore-arc peridotites, Fig. 6a;[38] and characterizes ED ophiolitic ultramafites [15, 17, 19, 36]. In terms of $Al_2O_3/SiO_2$ and $MgO/SiO_2$ ratios, they are like Arabian–Nubian shield and fore-arc peridotites (Fig. 6b; [13, 15, 28, 39, 40], low value of $Al_2O_3/SiO_2$ (fore-arc field), suggesting that these rocks were derived from a mantle source with high degrees of partial melting. The studied serpentinites have enriched compatible trace elements (Cr=2426–2709 ppm, Ni=1657–2377 ppm and Co=117–167 ppm) suggesting derivation from a depleted mantle peridotite source.

The SH mantle rocks are highly depleted in incompatible trace elements relative to the primitive mantle (Fig. 6c). They are variably depleted in Nb consistent with SSZ geochemical characteristics [41] similar to abyssal and fore-arc peridotites [42, 43]. Moreover, the positive Pb-anomaly on spider diagrams resembles abyssal and fore-arc peridotites [42, 43] (Fig.6c). This specific positive Pb-anomaly may proposes a protolith origin or reflects the result of fluid percolation during serpentinization processes [44, 45]. The serpentinites has low concentrations HFSE such as Nb, Hf, Ta, Ce, U and Th, comparatively high concentration of LILE such as Ba and Sr. Subduction zone trace element signatures are clear due to the enrichment of LILE (Sr and Ba) over HFSE (Nb, Ti, Y, Ce, U and HF) and negative Ta anomaly [22]. The REE diagram displays HREE enrichment and LREE depletion. The Av.ΣREE contents of serpentinites is 1.33 ppm.

Chondrite normalized REE patterns show very low fractionated patterns (La/Yb) = (1.398). The LREE of the studied ultramafic show a low degree of fractionation (La/Sm=1.24). The degree of fractionation of HREE is also low (Gd/Yb=0.998), (Fig.6d).

Preprints (www.preprints.org) | NOT PEER-REVIEWED | Posted: 8 October 2019 doi:10.20944/preprints201910.0079.v1



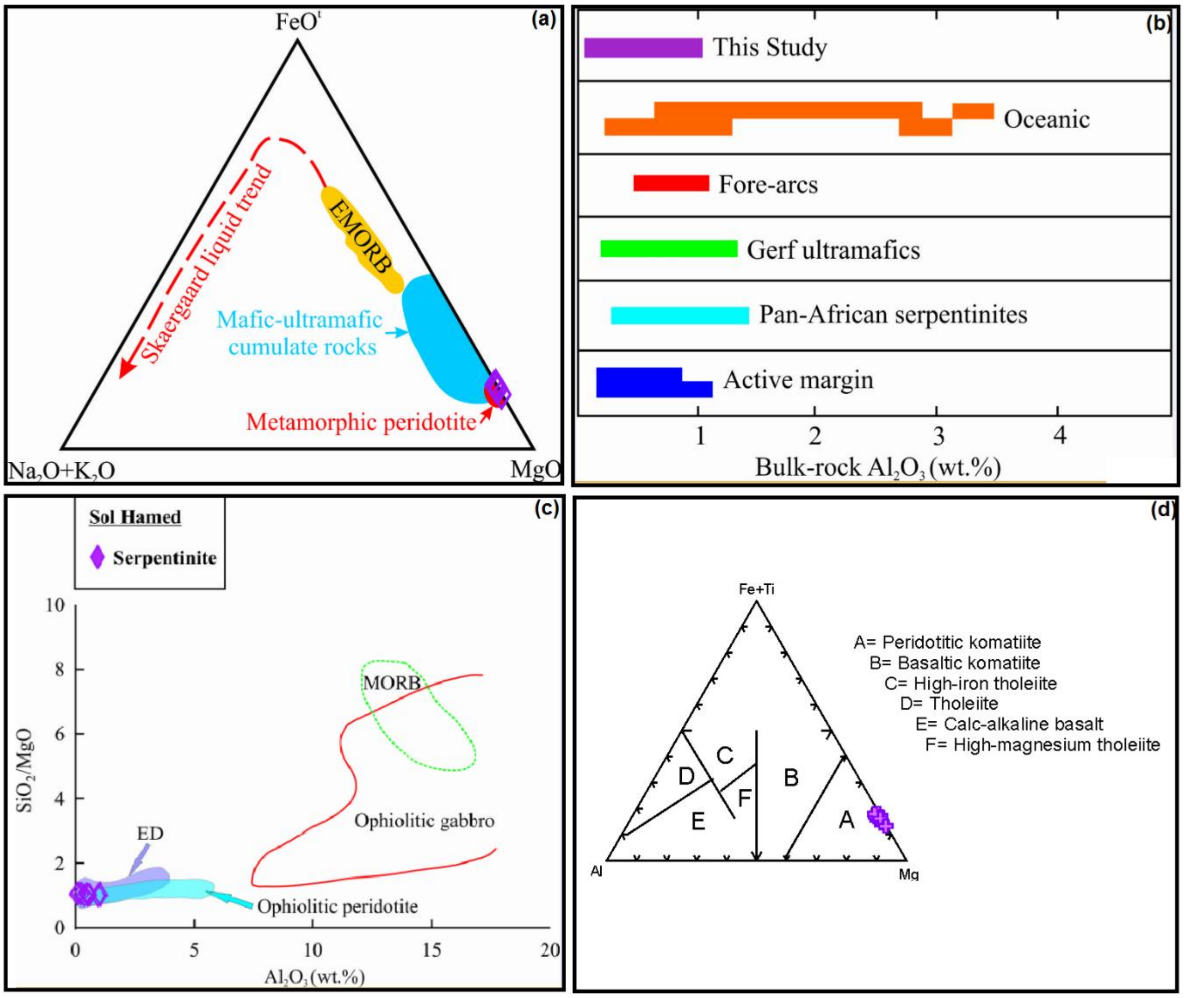


**Figure 5**. a) AFM diagram for SH serpentinites after [32], b) Bulk-rock $Al_2O_3$ (wt. %) contents of SH compared with those from other tectonic settings from [34] and the Pan-African serpentinites [18, 33], c) $SiO_2$/MgO ratios vs. $Al_2O_3$ diagram. Ophiolitic peridotite, ophiolitic gabbro and MORB are from [35]. Data from Eastern Desert (ED) are shown for comparison [13, 15, 17, 19, 36] and d) Jensen's cation plot after [37].

 doi:10.20944/preprints201910.0079.v1



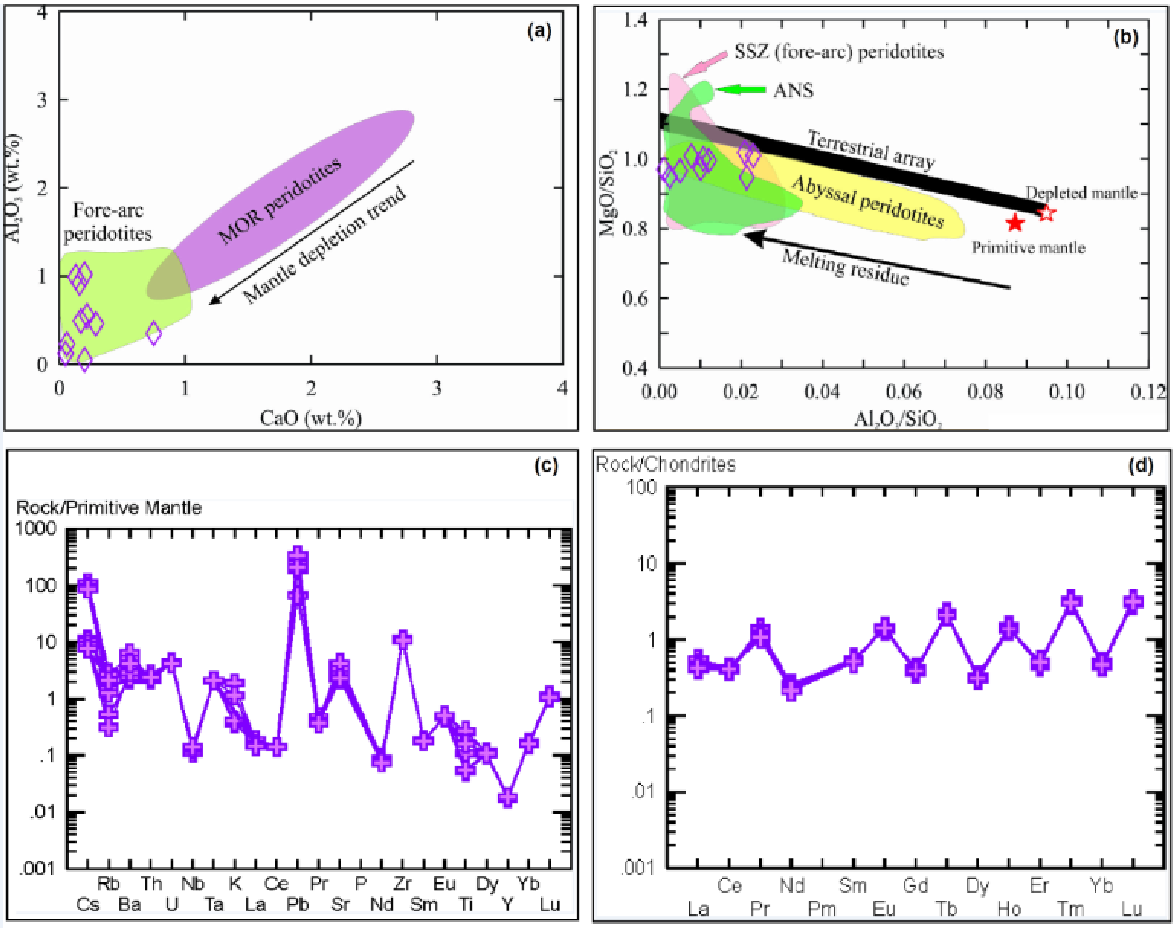


**Figure 6**. a) CaO vs. Al2O3 diagram showing SH serpentinites compared with fore-arc and MOR peridotites after [38] , b) MgO/SiO2 vs. Al2O3/ SiO2 diagram. Primitive and depleted mantle values are after [78] and [65], respectively. The "terrestrial array" represents the bulk silicate Earth evolution [79, 80] . Abyssal and fore-arc peridotite fields are after [28, 39, 42]. ANS ophiolitic peridotite field is after [13, 40] , c) Primitive mantle-normalized trace element patterns, and d) Chondrite-normalized REE patterns for the SH mantle section. Normalizing values are after [78].

## 6. Discussion

Metamorphism ranging from low-grade greenschist to medium-grade amphibolite facies usually influenced the ophiolitic ultramafites of the Egyptian ED forming serpentinite and/or mixtures of serpentine, talc, chlorite, carbonates and magnetite e.g., [13, 15, 46-48]. The time and source of carbonate metasomatism that commonly affected the Egyptian ultramafites still debated. [31] adopted mixing between mantle-derived $CO_2$-rich fluids and remobilized sedimentary carbonate. [49] suggested pure $CO_2$-bearing mantle source based on stable isotopes (i.e. O, C). Moreover, $CO_2$

Preprints (www.preprints.org) | NOT PEER-REVIEWED | Posted: 8 October 2019 doi:10.20944/preprints201910.0079.v1



input from mantle and metamorphic-degassing was proposed to explain the origin of the magnesite veins in serpentinites from the ED e.g., [50, 51] . Even with changes occurred during serpentinization in the mineral compositions of peridotites, geochemical data of serpentinites suggest negligible modification of major elements (except for Ca) at the hand-specimen scale e.g., [30, 45, 52]. Therefore, the low CaO contents (0.05–0.75 wt. %) in the serpentinites indicate restricted effect of Ca–metasomatism. The CaO contents are not correlated with LOI further confirming this implication. Moreover, the trace element compositions (except U and Sr) are not significantly modified during serpentinization e.g, [42, 45, 53]. Accordingly, the major and trace element data reflect the primary signature of the serpentinites protolith in subduction zones [45, 54, 55]. LOI reach up to 10.34-13.92 wt. %, which supports the role of hydrothermal alteration. In the $MgO$-$Fe_2O_3^T$-$Al_2O_3$ ternary diagram of [56], all samples plot in the metamorphic metasomatic field (Fig. 7a).

The $MgO/SiO_2$ and $Al_2O_3/SiO_2$ ratios of serpentinites agree with SSZ peridotites from fore-arc setting, Fig. 6b; [28, 39]. In the Hf-Th-Nb diagram [57] used to regulate the tectonic character of ultramafic rocks, all samples plot in the destructive field of plate margins (Fig. 7b). Generally, the $Al_2O_3$ and CaO depletion characterizes fore-arc peridotites (Fig. 6a) [29, 38]. The Cr vs. $TiO_2$ diagram also supports the SSZ setting for the SH serpentinites, Fig. 7c; [58].

The studied rocks show low $Al_2O_3$ content reflecting depleted upper mantle source [29]. Their high Mg#, Cr and Ni are consistent with a depleted mantle peridotite source [15, 59]. The $MgO/SiO_2$ and $Al_2O_3/SiO_2$ ratios (Fig. 6b) accord with peridotites generated from subduction-related magma source. It is supporting by using Zr vs. Nb binary diagram [60], all samples plot in the depleted mantle sources (Fig. 7d). Comparing SH ophiolites with other ophiolites such as, Troodos in Cyprus, [61], Gerf ophiolite in South Eastern Desert [15] and Wadi Ghadir ophiolites in Central Eastern Desert [22]. Using the criteria in [58] , we conclude that the chemical signature, the crystallization arrangement and mantle residue of SH ophiolites are similar to supra-subduction zone ophiolites formed in fore-arc basins based on the Ti–V variation diagram [62], (Fig. 7e).

Numerous geochemical studies demonstrated restricted mobility of major elements during serpentinization and protolith primary signature were retained e.g. [45, 52, 63] . The SH serpentinites have low CaO contents comparable to ophiolitic peridotites [35]. Moreover, their low $Al_2O_3$/ $SiO_2$ ratios (mostly $< 0.03$) are similar to fore-arc mantle wedge serpentinites suggesting that their protoliths had experienced partial melting before serpentinization which has no effect on this ratio e.g., [45, 53, 64]. Also, their low $MgO/SiO_2$ ratios (< 1.1) resemble serpentinised lherzolites and harzburgite [45]. They have low $TiO_2$ contents (0.01–0.06 wt. %) compared to depleted mantle composition but like subduction zone serpentinites [45, 65]. Their major element data consistent with harzburgitic source (Fig. 7f).

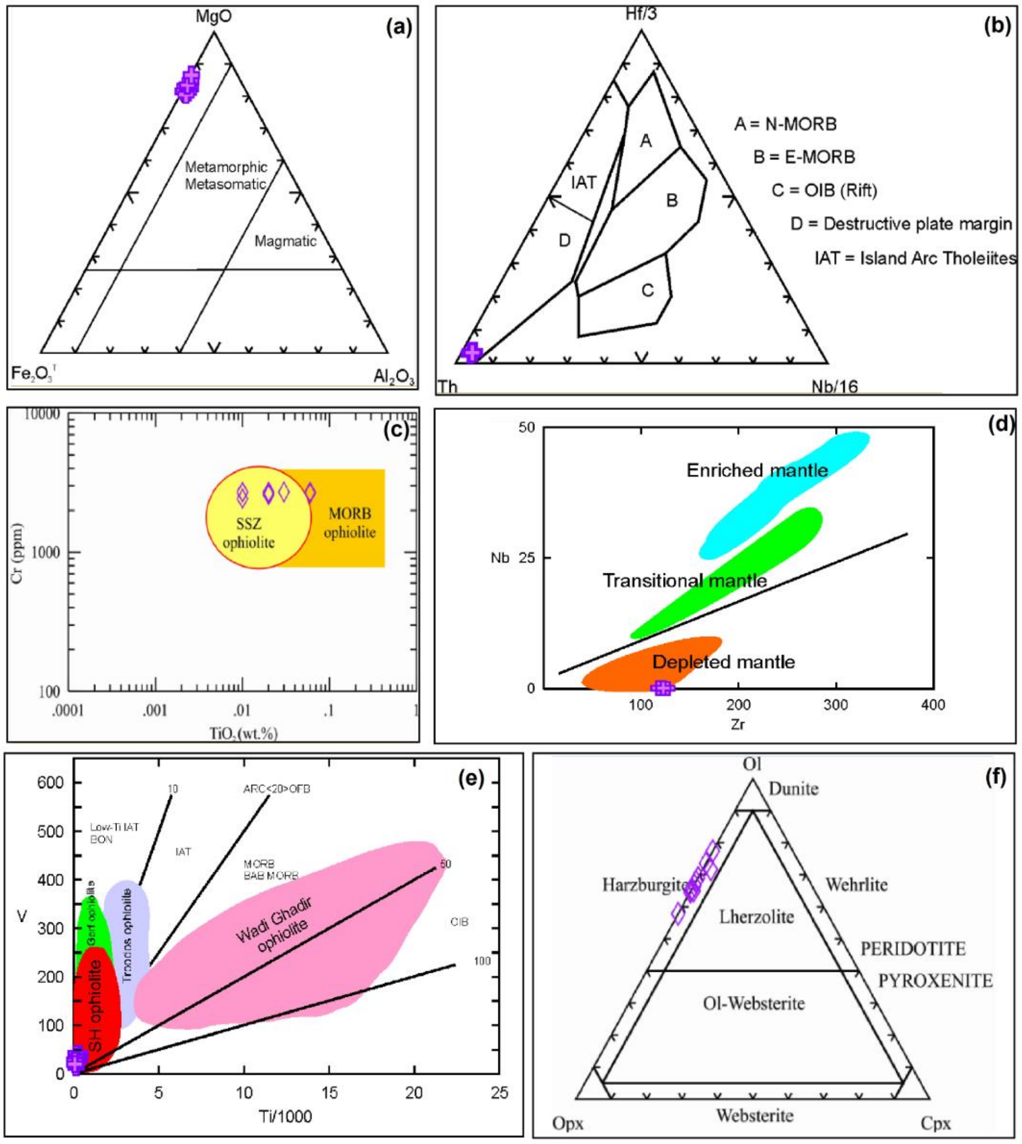


**Figure 7.** a) $MgO$-$Fe_2O_3^T$-$Al_2O_3$ ternary diagram for the ultramafic rocks. Zone after [56] and lines after [81], b) Hf/3-Th-Nb/16 ternary diagram of [57], c) Cr vs. $TiO_2$ plot to discriminate SSZ and MORB ophiolites after [58], d) Zr vs. Nb diagram after [60], e) Ti–V discrimination diagram [62], where Sol Hamed (SH) ophiolites (Red )compare with forearc/arc ophiolites, Troodos (blue) ophiolite from [61], Gerf (Green) ophiolite from [15] and Wadi Ghadir ophiolites (Pink) from [22] and f) Ol–Cpx–Opx diagram [82].

 doi:10.20944/preprints201910.0079.v1



Table (1) Major , trace and rare earth elements of the studied rocks.

| Sample no | 1 | 2 | 3 | 4 | 5 | 6 | 7 | 8 | 9 | 10 |
|---|---|---|---|---|---|---|---|---|---|---|
| Major oxides (wt. %) | | | | | | | | | | |
| $SiO_2$ | 45.699 | 46.286 | 45.709 | 45.539 | 45.957 | 45.654 | 44.360 | 44.050 | 44.857 | 47.617 |
| $TiO_2$ | 0.057 | 0.056 | 0.011 | 0.058 | 0.012 | 0.023 | 0.023 | 0.023 | 0.035 | 0.012 |
| $Al_2O_3$ | 0.550 | 0.993 | 0.491 | 0.465 | 0.046 | 0.231 | 1.015 | 0.915 | 0.346 | 0.115 |
| $Fe_2O_3{}^T$ | 7.788 | 8.365 | 7.771 | 9.294 | 9.099 | 9.799 | 9.249 | 9.954 | 8.660 | 6.924 |
| MnO | 0.103 | 0.089 | 0.114 | 0.081 | 0.092 | 0.173 | 0.056 | 0.034 | 0.104 | 0.104 |
| MgO | 45.470 | 43.832 | 45.709 | 44.261 | 44.575 | 44.063 | 44.778 | 44.863 | 45.226 | 45.182 |
| CaO | 0.218 | 0.134 | 0.171 | 0.290 | 0.196 | 0.058 | 0.203 | 0.160 | 0.750 | 0.046 |
| $Na_2O$ | 0.103 | 0.190 | 0.011 | 0.012 | 0.012 | 0.000 | 0.282 | 0.000 | 0.012 | 0.000 |
| $K_2O$ | 0.011 | 0.056 | 0.011 | 0.000 | 0.012 | 0.000 | 0.034 | 0.000 | 0.012 | 0.000 |
| Total | 100 | 100 | 100 | 100 | 100 | 100 | 100 | 100 | 100 | 100 |
| LOI | 12.690 | 10.340 | 12.490 | 13.920 | 13.180 | 13.260 | 11.340 | 12.600 | 13.280 | 13.350 |
| $SiO_2/MgO$ | 1.005 | 1.056 | 1.000 | 1.029 | 1.031 | 1.036 | 0.991 | 0.982 | 0.992 | 1.054 |
| $Al_2O_3/SiO_2$ | 0.012 | 0.021 | 0.011 | 0.010 | 0.001 | 0.005 | 0.023 | 0.021 | 0.008 | 0.002 |
| $MgO/SiO_2$ | 0.995 | 0.947 | 1.000 | 0.972 | 0.970 | 0.965 | 1.009 | 1.018 | 1.008 | 0.949 |
| Mg# | 92.077 | 91.247 | 92.131 | 90.450 | 90.692 | 89.940 | 90.592 | 89.961 | 91.220 | 92.855 |
| Trace elements (ppm) | | | | | | | | | | |
| V | 40.200 | 29.500 | 27.400 | 37.200 | 26.100 | 22.160 | 40.200 | 14.010 | 34.100 | 19.500 |
| Cr | 2655.400 | 2701.100 | 2706.600 | 2656.800 | 2688.800 | 2580.200 | 2701.200 | 2654.100 | 2708.600 | 2425.900 |
| Ni | 2377.100 | 1800.300 | 2056.300 | 2057.300 | 2070.100 | 1840.200 | 1816.200 | 2055.400 | 1657.200 | 1999.100 |
| Cu | 63.100 | 15.100 | 24.100 | 50.530 | 43.210 | 53.210 | 54.210 | 8.290 | 47.310 | 33.510 |
| Zn | 56.900 | 13.460 | 24.900 | 23.070 | 35.100 | 17.900 | 34.800 | 17.200 | 11.890 | 23.050 |
| Co | 166.500 | 121.400 | 120.500 | 162.300 | 165.200 | 152.400 | 154.200 | 152.400 | 117.200 | 136.100 |
| Ga | 1.560 | 1.050 | 0.900 | 1.300 | 1.200 | 1.110 | 1.200 | 1.400 | 1.330 | 1.340 |
| Rb | 0.330 | 0.350 | 0.500 | 0.400 | 0.450 | 0.500 | 0.450 | 0.350 | 0.300 | 0.280 |
| Sr | 55.020 | 46.150 | 47.900 | 62.100 | 60.100 | 72.110 | 50.100 | 88.990 | 48.080 | 48.100 |
| Zr | 120.000 | 118.000 | 127.000 | 119.000 | 121.000 | 120.000 | 123.000 | 122.000 | 121.000 | 118.000 |
| Nb | 0.100 | 0.090 | 0.085 | 0.100 | 0.100 | 0.100 | 0.090 | 0.080 | 0.090 | 0.100 |
| Ba | 35.600 | 15.100 | 25.000 | 15.120 | 19.800 | 17.110 | 16.430 | 45.040 | 20.000 | 29.500 |
| La | 0.100 | 0.100 | 0.100 | 0.100 | 0.100 | 0.100 | 0.100 | 0.100 | 0.100 | 0.100 |
| Ta | 0.085 | 0.085 | 0.085 | 0.085 | 0.085 | 0.085 | 0.085 | 0.085 | 0.085 | 0.085 |
| Pb | 4.800 | 13.140 | 16.100 | 15.100 | 16.900 | 19.900 | 17.100 | 4.660 | 24.050 | 14.700 |
| Th | 0.200 | 0.200 | 0.200 | 0.200 | 0.200 | 0.200 | 0.200 | 0.200 | 0.200 | 0.200 |
| Tl | 0.037 | 0.038 | 0.040 | 0.300 | 0.260 | 0.040 | 0.038 | 0.040 | 0.300 | 0.280 |
| Li | 10.100 | 5.000 | 7.000 | 6.120 | 5.500 | 8.200 | 8.980 | 9.900 | 1.710 | 7.150 |
| Hf | 0.020 | 0.020 | 0.020 | 0.020 | 0.020 | 0.020 | 0.020 | 0.020 | 0.020 | 0.020 |
| Cs | 0.850 | 0.750 | 0.090 | 0.090 | 0.088 | 0.090 | 0.080 | 0.680 | 0.070 | 0.060 |
| Sn | 0.085 | 0.085 | 0.085 | 0.085 | 0.085 | 0.085 | 0.085 | 0.085 | 0.085 | 0.085 |
| Bi | 0.010 | 0.030 | 0.025 | 0.020 | 0.010 | 0.020 | 0.030 | 0.030 | 0.025 | 0.020 |
| Cd | 2.100 | 2.100 | 3.200 | 3.400 | 2.150 | 2.500 | 3.500 | 3.400 | 3.450 | 2.900 |
| In | 0.010 | 0.010 | 0.010 | 0.010 | 0.010 | 0.010 | 0.010 | 0.010 | 0.010 | 0.010 |
| W | 0.090 | 0.090 | 0.090 | 0.090 | 0.090 | 0.090 | 0.090 | 0.090 | 0.090 | 0.090 |
| Mo | 0.010 | 0.010 | 0.010 | 0.010 | 0.010 | 0.010 | 0.010 | 0.010 | 0.010 | 0.010 |
| Re | 0.003 | 0.003 | 0.003 | 0.003 | 0.003 | 0.003 | 0.003 | 0.003 | 0.003 | 0.003 |
| Sb | 1.830 | 2.400 | 3.110 | 1.140 | 3.150 | 2.700 | 3.100 | 3.100 | 1.980 | 2.330 |
| As | 4.210 | 5.330 | 3.700 | 5.700 | 5.300 | 4.800 | 4.500 | 5.210 | 4.910 | 3.800 |
| Ag | 185.000 | 190.000 | 195.000 | 191.000 | 187.000 | 170.000 | 193.000 | 192.000 | 190.000 | 194.000 |
| S | 0.040 | 0.040 | 0.040 | 0.040 | 0.040 | 0.040 | 0.040 | 0.040 | 0.040 | 0.040 |
| Se | 0.300 | 0.500 | 0.400 | 0.300 | 0.700 | 0.230 | 0.300 | 0.400 | 0.700 | 0.500 |
| Be | 0.850 | 0.700 | 0.900 | 0.850 | 0.900 | 0.900 | 0.800 | 0.700 | 0.700 | 0.800 |
| Te | 5.500 | 5.400 | 5.500 | 5.500 | 4.110 | 4.800 | 5.700 | 4.300 | 4.980 | 5.120 |
| Rb | 1.810 | 1.000 | 1.200 | 1.700 | 1.450 | 1.700 | 0.330 | 0.800 | 0.200 | 1.300 |
| Sc | 4.100 | 4.010 | 3.800 | 3.550 | 4.200 | 3.700 | 3.940 | 4.010 | 4.300 | 3.900 |
| U | 0.090 | 0.090 | 0.090 | 0.090 | 0.090 | 0.090 | 0.090 | 0.090 | 0.090 | 0.090 |
| Rare earth elements (ppm) | | | | | | | | | | |
| Y | 0.080 | 0.080 | 0.080 | 0.080 | 0.080 | 0.080 | 0.080 | 0.080 | 0.080 | 0.080 |
| Ce | 0.250 | 0.249 | 0.248 | 0.250 | 0.250 | 0.250 | 0.250 | 0.250 | 0.250 | 0.250 |
| Dy | 0.079 | 0.082 | 0.080 | 0.080 | 0.080 | 0.080 | 0.080 | 0.080 | 0.080 | 0.080 |
| Eu | 0.078 | 0.080 | 0.080 | 0.080 | 0.080 | 0.080 | 0.080 | 0.080 | 0.080 | 0.080 |
| Er | 0.078 | 0.084 | 0.080 | 0.080 | 0.080 | 0.080 | 0.080 | 0.080 | 0.080 | 0.080 |
| Gd | 0.081 | 0.077 | 0.080 | 0.080 | 0.080 | 0.080 | 0.080 | 0.080 | 0.080 | 0.080 |
| Ho | 0.083 | 0.078 | 0.080 | 0.080 | 0.080 | 0.080 | 0.080 | 0.080 | 0.080 | 0.080 |
| Nd | 0.100 | 0.100 | 0.100 | 0.100 | 0.100 | 0.100 | 0.100 | 0.100 | 0.100 | 0.100 |
| Pr | 0.100 | 0.120 | 0.100 | 0.100 | 0.100 | 0.100 | 0.100 | 0.100 | 0.100 | 0.100 |
| Sm | 0.083 | 0.079 | 0.082 | 0.083 | 0.078 | 0.078 | 0.079 | 0.084 | 0.083 | 0.078 |
| Tm | 0.077 | 0.081 | 0.080 | 0.080 | 0.080 | 0.080 | 0.080 | 0.080 | 0.080 | 0.080 |
| Tb | 0.080 | 0.079 | 0.080 | 0.080 | 0.080 | 0.080 | 0.080 | 0.080 | 0.080 | 0.080 |
| Yb | 0.083 | 0.077 | 0.080 | 0.080 | 0.080 | 0.080 | 0.080 | 0.080 | 0.080 | 0.080 |
| Lu | 0.082 | 0.076 | 0.080 | 0.080 | 0.080 | 0.080 | 0.080 | 0.080 | 0.080 | 0.080 |
| ΣREE | 1.334 | 1.342 | 1.330 | 1.333 | 1.328 | 1.328 | 1.329 | 1.334 | 1.333 | 1.328 |
| La/Yb | 1.325 | 1.429 | 1.538 | 1.688 | 1.310 | 1.205 | 1.358 | 1.410 | 1.447 | 1.266 |
| Gd/Yb | 0.976 | 1.000 | 1.000 | 1.000 | 1.000 | 1.000 | 1.000 | 1.000 | 1.000 | 1.000 |
| La/Sm | 1.205 | 1.266 | 1.220 | 1.205 | 1.282 | 1.282 | 1.266 | 1.190 | 1.205 | 1.282 |

Preprints (www.preprints.org) | NOT PEER-REVIEWED | Posted: 8 October 2019 doi:10.20944/preprints201910.0079.v1



## 7. Structural setting

### 7.1. Deformation history

The structure of the SH area is complex, and partially agreed [26], the area situated in a supra-structural position between three major Pan-African terranes (SE Desert, Gabgaba, and Gebeit terranes). Four deformational events can be distinguished in the Neoproterozoic rocks [66-69];

- **$D_1$** event: E–W thrust faults and related E–W (F1) folds which considered as early stages of collision of Gerf and Gabgaba arc terranes.
- **$D_2$** event: NW–SE thrust faults and related NW–SE (F2) folds were formed, characterized by local high-P, low-T metamorphism and reflected as late stages of collision of Gerf and Gabgaba arc terranes. The mineralization in this stage is described as remobilization of Cu–Ni–Pt sulfides in ultramafic rocks, alteration talc/serpentinites and listwaenites; Talc carbonate, gold-bearing quartz veins.
- **$D_3$** event: conjugate NNW-trending sinistral and NNE-trending dextral transpression, as well as N–trending tight folds (F3). NW–SE shear zones and open folds, crenulation cleavage, SC fabrics, sigmoidal foliation patterns that defined in late- to post-tectonic granitoids. This stage characterized by local contact metamorphism. The mineralization in this stage is styled as kaolinitized alteration zones along D3, shear zones; ferregination and silicification of copper sulfide zones and gold–quartz veins. Shortening connected to collision of east and west Gondwana; tectonic escape toward oceanic free face to N along WNW striking Najd faults.
- **$D_4$** event: E–W dextral strike-slip and dip-slip normal faults striking NNW–SSE to N–S and E–W may be related to Red Sea rifting. This stage characterized by dike swarms along faults. The mineralization in this stage is styled as disseminated secondary uranium and anomalous secondary concentrations of Pb, Zr, Y, Nb, Ta, in late dikes.

### 7.2. Faults and structural analysis

The SH complex is characterized by flat-lying and steeply dipping ductile shear zones trending ENE and associated thrust sheets (Fig. 2, 8a). The strike-slip shear zones which surround the SH to the N and S show tectonic transport to the ENE where SH mass movement in this direction generated over thrusts of the SH on the volcanic–sedimentary succession. The ENE tectonic direction transport is inferred from moderately-plunging WSW-directed mineral lineation, rodding, minor

Preprints (www.preprints.org) | NOT PEER-REVIEWED | Posted: 8 October 2019 doi:10.20944/preprints201910.0079.v1



fold axes and from long axes of the deformed pillows. Shears and thrust planes are characterized by either siliceous mylonites or talc iron rich schists and ankerite-carbonates.

There are three major faults on the investigated area (Fig. 8b).

- The first is NE-SW trending faults and is mainly present in the volcanic-sedimentary assemblage and Gabal SH.
- The second is E-W faulting affects all the basement rocks and disturbs the NE-SW trending faults.
- The third is N-S faults are probably related to some stages of the Red Sea rifting, and affected all the rock units including sandstone and Quaternary marine sediments of the Red Sea coast.

The direction of the shear zone on the investigated area has NE, the principal stress access has WNW to EW (Fig. 8a). The associated structural features are signified by:

- NNE-SSW normal faults,
- NW-SE reverse faults,
- NE-SW, NW-SE, WNW-ESE, NNE-SSW and EW quartz veins (Fig. 8c).

The mineralized structures (Fig. 8d), are represented by

- Quartz veins have mainly NE-SW and NNW-SSE trends
- Faults have mainly NE-SW trends
- Breccia and alteration has mainly NW-SE trend

El Sela shear zone is separated by two main faults in the direction of ENE–WSW and NNW–SSE (Fig. 2). The earlier trend associated with the major shear zone is injected by quartz veins. This shear zone is dissected into three parts by two strike slip faults trending NNW–SSE. Field observations indicate that the granites are affected by different stages of alteration, mainly at El Sela shear zone. These granites are invaded by ENE–WSW quartz veins. These veins caused hydrothermal alteration associated with radioactive mineralization in the fine-grained granites. Secondary uranium mineralization is observed as canary-yellow thin layers deposited along small cracks and micro-fractures.

**7.3. Kinematic indicators**

doi:10.20944/preprints201910.0079.v1



Various kinematic indicators are used to fix the sense of movement with the common settled in the brittle-ductile system. The most common kinematic indicators on the SH area are mylonites (Fig. 9a) and quartz fish (Fig. 9b) shows dextral sense of movement. Mylonites take place in extraordinary strain zones (mylonite zones) and are understood as exhumed ductile shear zones. The sense of replacement on a shear zone is usually expected to lie subparallel to striations, stretching and mineral lineations.

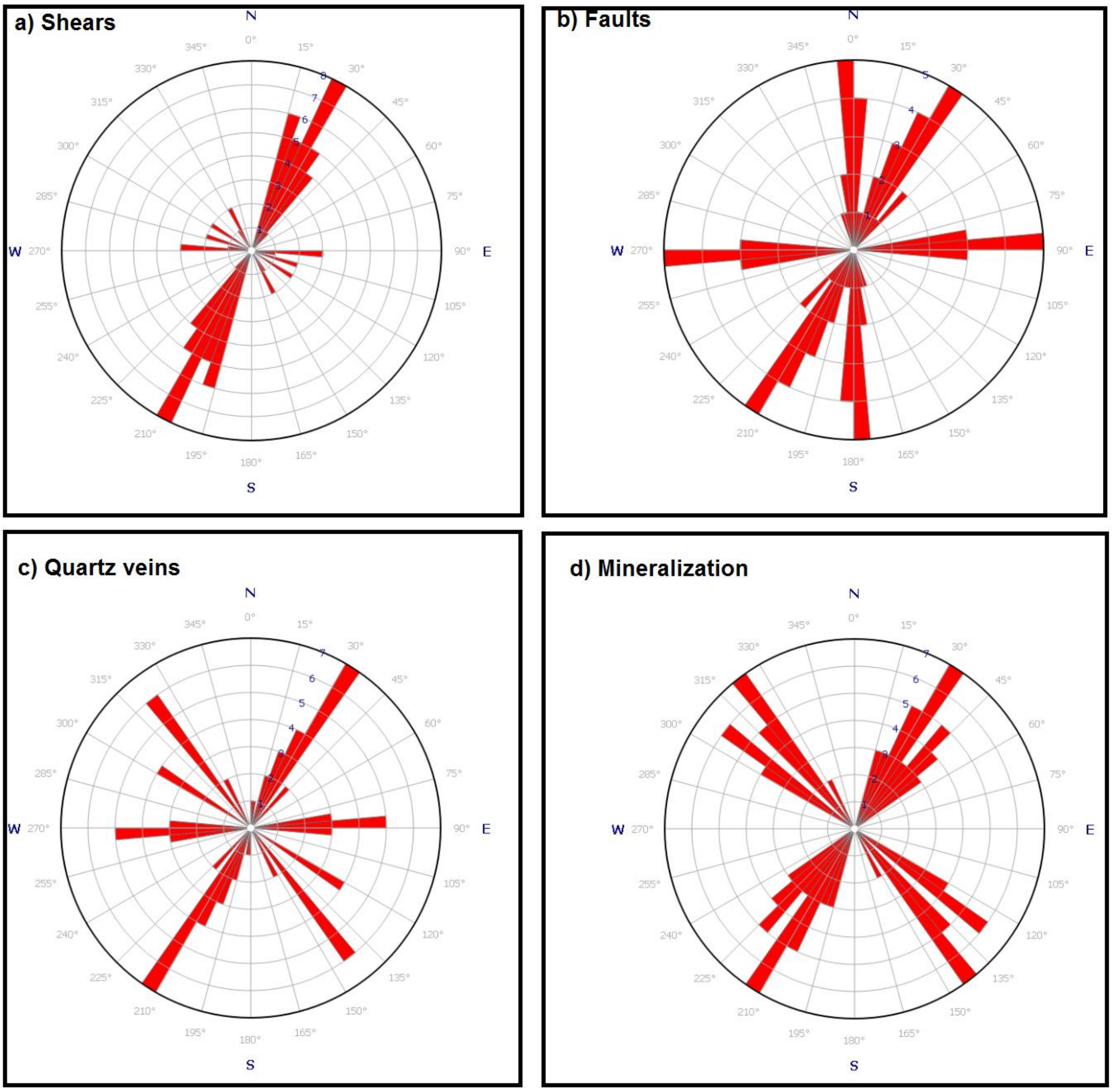


**Figure 8**. Structural analysis of Sul Hamid area.

 doi:10.20944/preprints201910.0079.v1



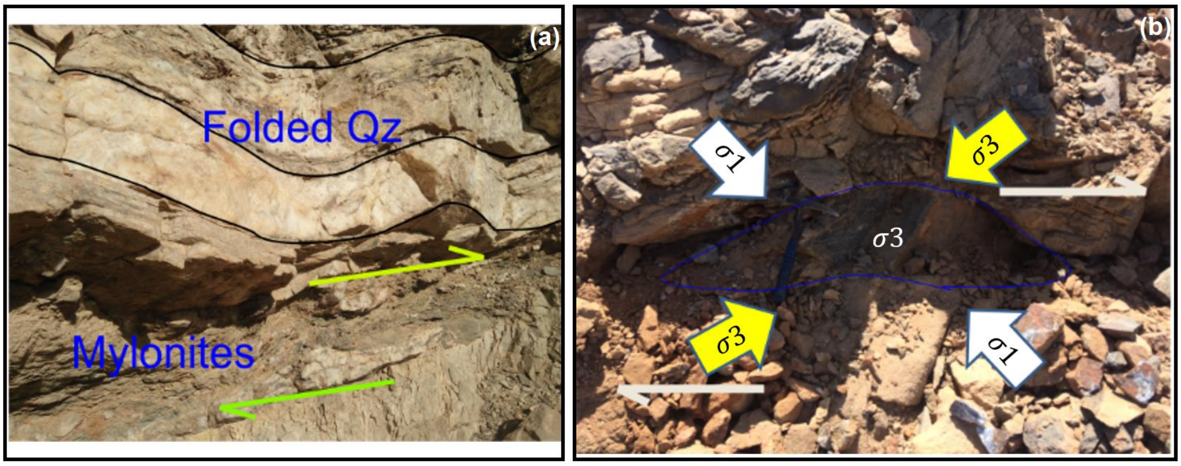


**Figure 9**. a) Mylonite derived from a narrow shear zone transecting a weakly deformed granodiorite. b) Quartz fish from a quartzite mylonite shows dextral sense of movement. Quartz in the matrix is dynamically recrystallized and developed an oblique foliation.

## 8. Ore mineralogy

The opaque mineral content in the studied rock types from 2% to 6% of the rock volume. They are represented by sulphides, magnetite, hematite and gold.

Sulphides minerals are mainly represented by arsenopyrite, pentlandite, pyrrhotite and pyrite. Minor crystals of chalcopyrite and bornite are observed in few samples. Arsenopyrite occurs as subhedral to euhedral rhombic crystals either independent or associated with pyrrhotite (Fig. 10a). It shows white color and displays strong anisotropism of blue color. Pentlandite occurs either as homogeneous or zoned grains (Fig. 10b). Pyrrhotite forms irregular grains with bluish shade and moderate reflectance and sometimes replaced by light creamy to yellow isotropic pentlandite (Fig 10a). Pyrite occurs as subhedral to euhedral crystals either replaced by magnetite (Fig. 10c). The replacement of pyrite by magnetite indicates oxidizing conditions.

Magnetite appears as anhedral crystals with peripheral granules of pyrite. Magnetite forms well-formed euhedral crystals of light grey color and moderate reflectance (Fig. 10c). Hematite exhibits whiter color and cherry red internal reflection. It shows isotropism in minor parts, which reveals its alteration from previous existing magnetite.

Gold is only recorded in highly altered quartz veins associated with the granitic masses. It occurs as disseminated grains that have bright yellow color with greenish tint. These grains occur as inclusions in arsenopyrite crystals (Fig.10d) and at pyrite-arsenopyrite contacts (Fig. 10e). The gold grains range in color from yellow to creamy yellowish color and with occur as sub-rounded grains or as straight-edged grains (Figs. 10d, e).

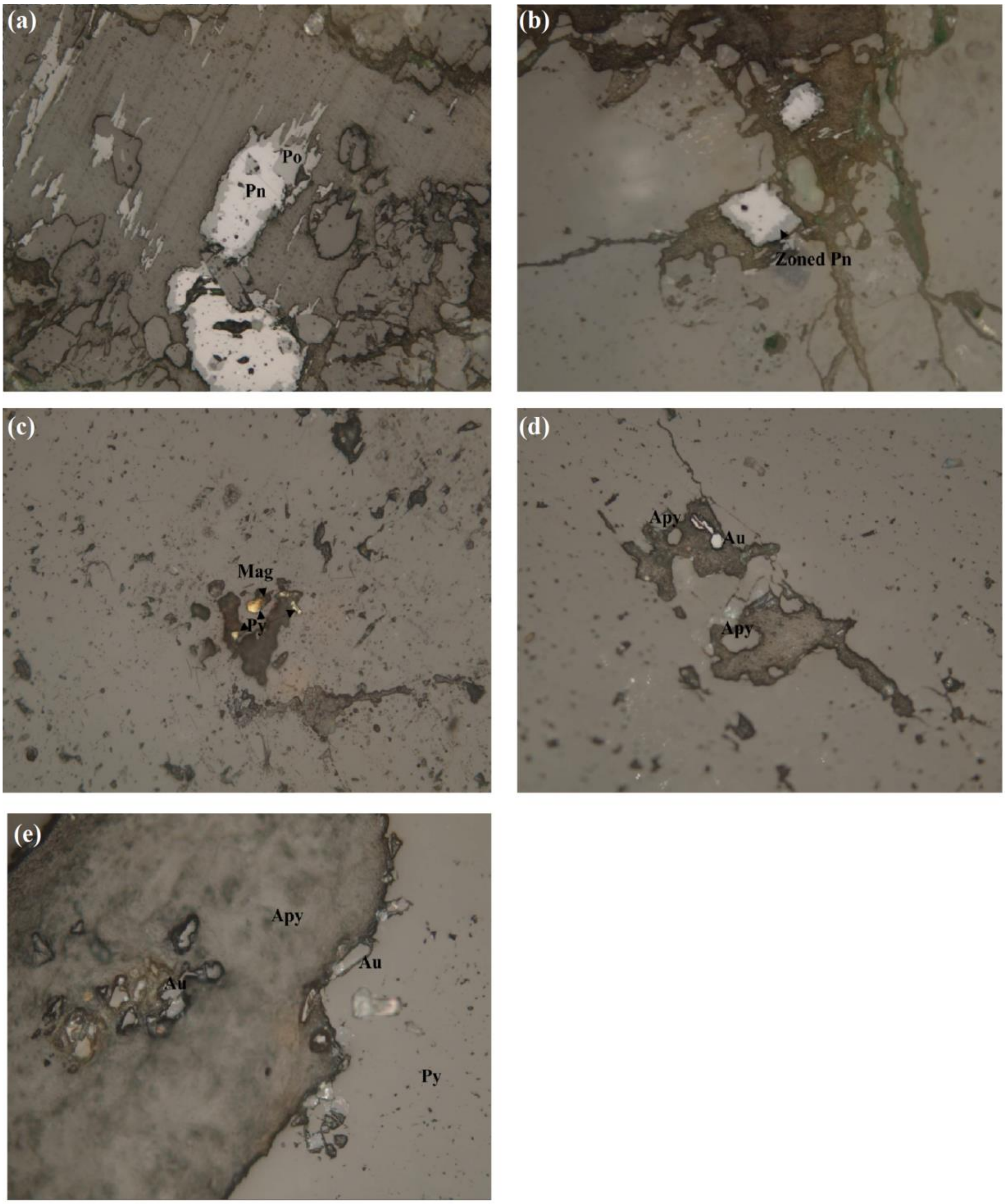


**Figure 10**. Photomicrograph showing a) Pyrrhotite forms irregular grains with bluish shade and moderate reflectance and sometimes replaced by light creamy to yellow isotropic pentlandite, b) Pentlandite occurs either as homogeneous or zoned grains, c) Magnetite forms well-formed euhedral crystals , d) Gold as inclusions in arsenopyrite crystals and e) Pyrite-arsenopyrite contacts and The gold grains range in color from yellow to creamy yellowish color and with occur as sub-rounded grains or as straight-edged grains.

Preprints (www.preprints.org) | NOT PEER-REVIEWED | Posted: 8 October 2019 doi:10.20944/preprints201910.0079.v1



## 9. Economic potentiality

### 9.1. Magnesite mineralization

Economically, the important magnesite deposits occur in two types: the Venarch and Kraubath type [70]. The Venarch type deposits have the world's largest reserves [70]. They form strata-bound lensoid bodies of coarsely crystalline spar-magnesite hosted by marine sediments. Genetically, they are associated with shallow marine water of chloride-type evaporites. Kraubath type deposits are cryptocrystalline magnesite [70] and less common than spar-magnesites. However, they are important because of their high quality magnesite product. These deposits comprise stock-works and veins of white magnesite formed in ultramafic country rocks. The origin of Kraubath magnesite type deposits favor hypogene-hydrothermal formation [70].

Magnesite deposits of SH serpentinites are cryptocrystalline formed by hydrothermal solution effects on the serpentinite host rocks and occur in three forms. The first is represented by white patches consisting of vertical veins and horizontal sheets. The second is found as veinlets represented by stock-work shape, characterized by nodules clusters and exposed as pockets within the serpentinites. The third is widespread in Wadi Diit NE of Gabal SH and is intercalated with surficial deposits. It is found as veinlets with stock-work shape and has low grade magnesite ore. These features are consistent with Kraubath type deposits (Fig. 11).

The magnesite pockets exposed at the NE ends of SH serpentinites and along NNE trending shear zone (Fig. 2). The magnesium source in magnesite is likely the magnesium-rich minerals (e.g., serpentine, olivine) occurred within ultramafics. Serpentinite appears to be the host for over 90 % of all known magnesite veins worldwide.

The chemical data of magnesite ore is recalculated and presented in Table 2. The collected samples contain average (wt. %) 42.98 MgO, 0.57 $SiO_2$, 0.09 $Fe_2O_3$, 4.5 CaO, and 0.023 $P_2O_5$. They show depletion in some incompatible major elements (i.e., Ca, Al and Na) relative to the average primitive composition of upper mantle [71]. Possibly some of this CaO might has been lost during serpentinization [72] and shows strongly negative correlation with MgO (Pearson correlation factor= -0.864) in Table 3. Iron also shows loss during serpentinization.

### 9.2. Gold deposits

Ophiolitic serpentinites surrounded the metavolcano-sedimentary assemblage are the likely sources for gold mineralization in the vein-type gold deposits which invaded the island-arc volcanic and volcaniclastic rocks and/or the granitic rocks [73, 74].

The vein-type mineralization occurred in the sheared ophiolitic serpentinites (Fig. 12a) associated with the Pan-African Orogeny. Linear zones of serpentinites display abundant alterations along thrusts and shear zones with the development of talc, talc-carbonate and reddish brown quartz-carbonate rock (i.e., listwaenite) (Fig. 12b). Listwaenite is commonly mineralized with gold [75, 76]. Malachite-bearing quartz veins with NW-SE direction cut through gabbroic rocks and show mylonitic structure, pinch and swell phenomenon. They are extremely fractured containing considerable content of malachite and disseminated sulfide minerals (Fig. 12c, f). Mineralized smoky quartz veins with NE-SW direction and steeply dipping SE invaded the meta-andesite (Fig. 12g). They are intensively sheared and contain iron oxides in the fissures and cracks (Fig. 12d, e, and f). The barren quartz veins are nearly vertical and have E-W directions (Fig. 12f). The highest gold grades are associated with strong arsenopyrite mineralization and in fracture-seal veins.

Mineralized alteration zones trending NW-SE and dipping nearly vertical traverse metagabbro and metavolcanics (Fig. 12f). They are characterized by the presence of hematite, limonite, goethite and fresh pyrite. They occur either neighboring the auriferous quartz veins. The common types of alteration are silicification, sulphidation, carbonatization, listwaenitization.

 doi:10.20944/preprints201910.0079.v1



Table 2. Magnesite chemical analysis :

| | 1 | 2 | 3 | 4 | 5 | 6 | 7 | 8 | 9 |
|---|---|---|---|---|---|---|---|---|---|
| $SiO_2$ | 0.70 | 0.68 | 0.40 | 1.30 | 0.23 | 0.30 | 0.90 | 0.30 | 0.30 |
| $TiO_2$ | 0.00 | 0.00 | 0.00 | 0.00 | 0.00 | 0.00 | 0.00 | 0.00 | 0.00 |
| $Al_2O_3$ | 0.10 | 0.10 | 0.10 | 0.10 | 0.10 | 0.10 | 0.10 | 0.10 | 0.10 |
| $Fe_2O_3$ | 0.04 | 0.05 | 0.10 | 0.32 | 0.03 | 0.06 | 0.05 | 0.05 | 0.06 |
| Fe | 0.03 | 0.03 | 0.07 | 0.22 | 0.02 | 0.04 | 0.03 | 0.04 | 0.04 |
| MnO | 0.00 | 0.00 | 0.00 | 0.00 | 0.00 | 0.00 | 0.00 | 0.00 | 0.00 |
| Mn | 0.00 | 0.00 | 0.00 | 0.00 | 0.00 | 0.00 | 0.00 | 0.00 | 0.00 |
| MgO | 42.70 | 42.30 | 42.60 | 41.10 | 45.50 | 43.00 | 45.10 | 43.40 | 41.10 |
| CaO | 5.80 | 5.18 | 5.50 | 5.18 | 1.60 | 5.30 | 2.60 | 4.18 | 5.30 |
| $Na_2O$ | 0.40 | 0.15 | 0.18 | 0.15 | 0.50 | 0.01 | 0.01 | 0.15 | 0.01 |
| $K_2O$ | 0.00 | 0.01 | 0.00 | 0.00 | 0.00 | 0.00 | 0.00 | 0.00 | 0.00 |
| P2O5 | 0.02 | 0.02 | 0.02 | 0.02 | 0.02 | 0.07 | 0.02 | 0.02 | 0.02 |
| LOI | 49.10 | 49.30 | 50.10 | 49.00 | 49.30 | 50.30 | 49.50 | 50.50 | 51.01 |
| Total | 98.89 | 97.82 | 99.07 | 97.40 | 97.30 | 99.19 | 98.31 | 98.74 | 97.94 |

Preprints (www.preprints.org) | NOT PEER-REVIEWED | Posted: 8 October 2019 doi:10.20944/preprints201910.0079.v1



Table 3: Pearson Correlations between oxides in magnesite mineralization

| | MgO | CaO | SiO2 | Na2O | K2O | P2O5 |
|---|---|---|---|---|---|---|
| MgO | 1 | | | | | |
| CaO | **-0.864** | 1 | | | | |
| SiO2 | -0.27 | 0.139 | 1 | | | |
| Na2O | 0.36 | -0.308 | -0.124 | 1 | | |
| K2O | -0.086 | 0.138 | -0.01 | -0.041 | 1 | |
| P2O5 | -0.047 | 0.254 | -0.236 | -0.316 | -0.052 | 1 |

511

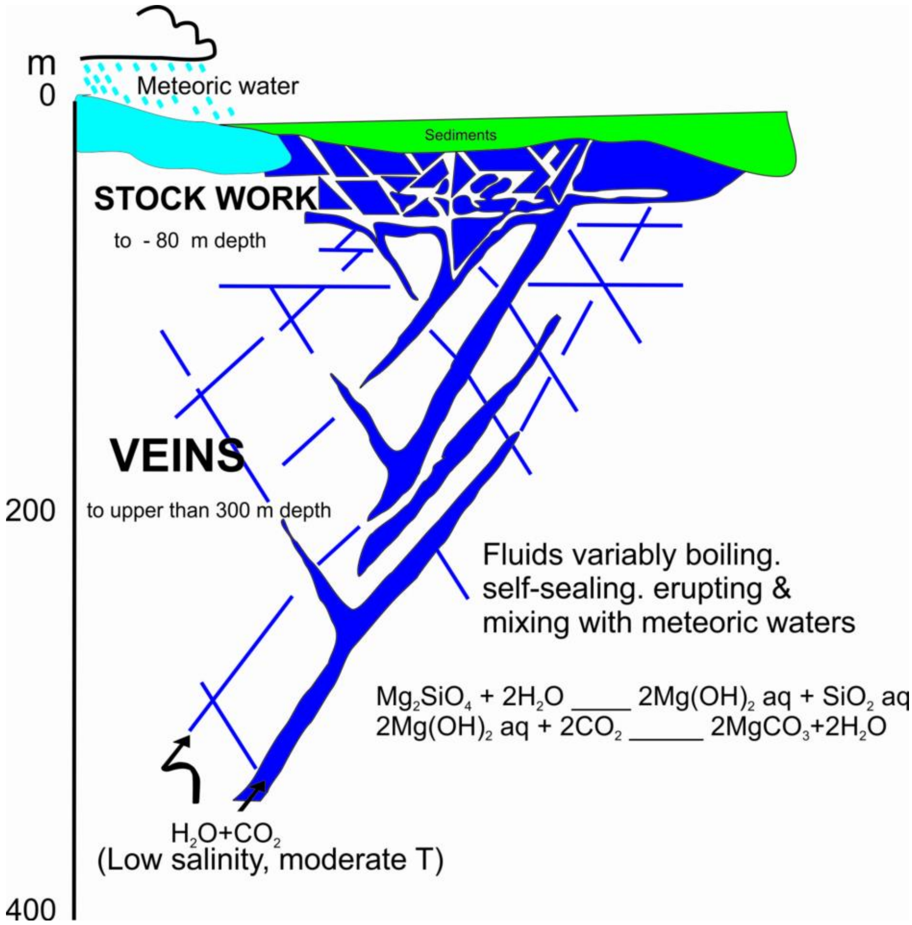


512

513 **Figure 11**. Kraubath type of magnesite deposit model after [83]

514

doi:10.20944/preprints201910.0079.v1



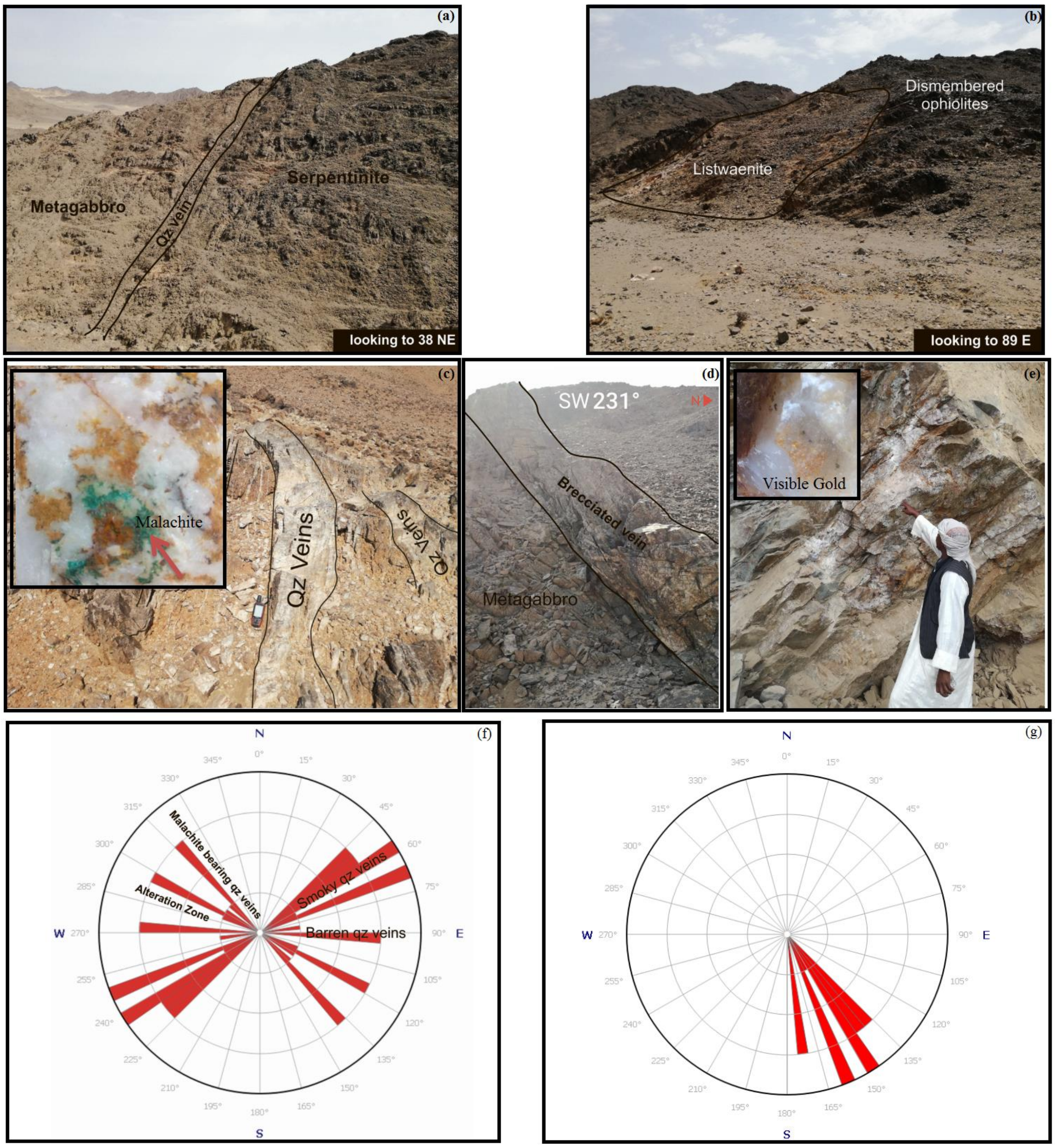


**Figure 12**. Field photographs show a) quartz vein between metagabbro and serpentinites, b)the listwaenite within dismembered serpentinite, c) Malachite-bearing quartz veins, d) Brecciated quartz vein containing iron oxides in the fissures, and e) Smoky quartz vein with visible gold. Rose diagram showing f) Alteration zone and various types of quartz veins, and g) the dipping of smoky quartz vein.

## 10. Conclusions

**a.** Sol Hamed (SH) area as a part of the ANS ophiolites occurred within Onib-Sol Hamed suture zone in the southern Eastern Desert of Egypt. The ophiolitic assemblages in this area are

Preprints (www.preprints.org) | NOT PEER-REVIEWED | Posted: 8 October 2019 doi:10.20944/preprints201910.0079.v1



represented by serpentinite, metagabbro and arc assemblages represented by metavolcanics. They later intruded by gabbroes and granites.

**b.** Geochemically, the compatible trace elements (Cr-Ni-Co) enrichment in SH serpentinites indicate derivation from a depleted mantle peridotite source. They show affinity to the typical metamorphic peridotites with peridotitic komatiite nature. The normative compositions reflect harzburgitic mantle source. Their $Al_2O_3$ contents (0.05–1.02 wt. %) are akin to oceanic and active margin peridotites and Pan-African serpentinites. The Cr and $TiO_2$ contents indicate SSZ environment with tectonic character destructive plate margins and depleted mantle sources. Their $Al_2O_3/SiO_2$ and $MgO/SiO_2$ ratios support the SSZ affinity and are similar to ANS peridotites with fore-arc setting. Low value of $Al_2O_3/SiO_2$ (fore-arc field), suggesting that these rocks were derived from a mantle source with high degrees of partial melting. Moreover, their $Al_2O_3$ and CaO depletion is typical of fore-arc peridotites. The normative compositions replicate harzburgitic mantle source.

**c.** Structurally, the area represents four deformational events can be distinguished in the Neoproterozoic rocks ($D_1$, $D_2$, $D_3$ and $D_4$); $D_1$: E–W thrust faults and related E–W ($F_1$) folds; $D_2$: NW–SE thrust faults and related NW–SE ($F_2$) folds were formed; $D_3$: conjugate NNW-trending sinistral and NNE-trending dextral transpression, as well as N–trending tight folds ($F_3$) and $D_4$: is E–W dextral strike-slip and dip-slip normal faults striking NNW–SSE to N–S and E–W may be related to Red Sea rifting. There are major three fault sets affected the area. The first set trend mainly NE-SW and is manifested in the volcanic-sedimentary assemblage and Gabal SH. The second set trend E-W affecting all the basement rocks and disturbs the first fault set. The third set trend N-S affected all the rock units.

The associated structural features with shearing are showed as fallowing:

- NNE-SSW normal faults,
- NW-SE reverse faults,
- NE-SW, NW-SE, WNW-ESE, NNE-SSW and EW quartz veins.

The mineralized structures are exemplified by

- Quartz veins have mainly NE-SW and NNW-SSE trends,
- Faults have mainly NE-SW trends,

- Breccia and alteration has mainly NW-SE trend.

**d.** Magnesite ore deposits in SH serpentinites is cryptocrystalline formed due to hydrothermal alteration of the serpentinite host rocks. It is occur as snow-white veins and stock-works. These characteristics are typical of Kraubath type magnesite deposits

**e.** Gold mineralization is confined to malachite-bearing quartz veins, smoky quartz veins and alteration zones. The gold grades increase with arsenopyrite occurrences.

**Acknowledgments**

The first author is grateful to Shalateen Mineral Resource Company and Gold Pyramids Group Company for helping during geologic field work. He also, thanked his mother and his wife for continuous support. And his first baby Sela.

**References**

1. Stern, R.J., *Neoproterozoic crustal growth: the solid Earth system during a critical episode of Earth history.* . Gondwana Research 2008. . **14,** : p. 33–50.
2. Stoeser, D.B., Camp, V.E., , *Pan-African microplate accretion of the Arabian Shield.* Geological Society of America Bulletin 1985. **96, x**: p. 96, 817–826.
3. Johnson, P.R., Woldehaimanot, B., , *Development of the Arabian–Nubian Shield: perspectives on accretion and deformation in the northern East African Orogen and the assembly of Gondwana. In: Yoshida, M., Dasgupta, S., Windley, B. (Eds.), Proterozoic East Gondwana: Supercontinent Assembly and Breakup.* Geological Society of London Special Publications, , 2003. . **206,** : p. pp. 289–325.
4. Stern, R.J., Johnson, P.J., Kröner, A., Yibas, B., , *Neoproterozoic ophiolites of the Arabian–Nubian Shield. In: Kusky, T. (Ed.),* . Precambrian Ophiolites. Elsevier, , 2004. : p. pp. 95–128.
5. Stern, R.J., *Crustal evolution in the East African Orogen: a neodymium isotopic perspective.* . Journal of African Earth Sciences 2002. . **34,** : p. 109–117.
6. Abu-Alam, T.S., and Hamdy, M. M., , *Thermodynamic modelling of Sol Hamed serpentinite, South Eastern Desert of Egypt: implication for fluid interaction in the Arabian–Nubian Shield ophiolites.* Journal of African Earth Sciences,, 2014. **v. 99,** : p. p. 7-23.

7. Stern, R.J., *Arc assembly and continental collision in the Neoproterozoic East African Orogen: implications for the consolidation of Gondwanaland.* . Annual Reviews of Earth and Planetary Science 1994. . **22,** : p. 319–351.

8. Jacobs, J., Thomas, R.J., , *Himalayan-type indenter-escape tectonics model for the southern part of the late Neoproterozoic–early Paleozoic East African-Antarctic orogen.* . Geology 2004. . **32,**: p. 721–724. .

9. Pallister, J.S., Stacey, J.S., Fischer, L.B., Premo, W.R., , *Precambrian ophiolites of Arabia; geologic setting, U–Pb geochronology, Pb-isotope characteristics, and implications for continental accretion.* . Precambrian Research, 1988. **38**: p. 1-54.

10. Kröner, A., Todt, W., Hussein, I.M., Mansour, M., Rashwan, A.A., , *Dating of late Proterozoic ophiolites in Egypt and the Sudan using the single grain zircon evaporation technique.* . Precambrian Research 1992. . **59,** : p. 15–32.

11. El-Bialy, M.Z., *On the Pan-African transition of the Arabian–Nubian Shield from compression to extension: the post-collision Dokhan volcanic suite of Kid-Malhak region, Sinai, Egypt.* . Gondwana Research 2010. . **17,** : p. 26–43.

12. Abdel-Salam, M.G., Tsige, L., Yihunie, T., Hussien, B., , *Terrane rotation during the East African Orogeny: evidence from the Bulbul Shear Zone, south Ethiopia.* . Gondwana Research 2008. . **14**: p. 497–508.

13. Abdel-Karim AM, A.S., El-Shafei SA *Mineral chemistry and geochemistry of ophiolitic metaultramafics from Um Halham and Fawakhir, Central Eastern Desert, Egypt* International Journal of Earth Sciences, , 2018. **107**: p. 2337–2355.

14. Abdel-Karim AM, A.S., El-Shafei SA *Mineral chemistry and geochemistry of ophiolitic ultramafics from central Eastern Desert, Egypt: a case for contaminated mantle-derived magma.* . Geophysical Research Abstracts 2017. **Vol. 19,** (EGU2017-16680-1, EGU General Assembly 2017).

15. Abdel-Karim AM, A.S., Helmy HM, El-Shafei SA *Fore-arc setting of the Gerf ophiolite, Eastern Desert, Egypt: evidence from mineral chemistry and geochemistry of ultramafites.* . Lithos 2016. **263**: p. 52–65

16. Ahmed AH, G.M., Arai S *Characterization of the thermally metamorphosed mantle–crust transition zone of the Neoproterozoic ophiolite at Gebel Mudarjaj, south Eastern Desert, Egypt.* . Lithos 2012. **142–143**: p. 67–83.
17. Azer, M.K., Stern, R.J., , *Neoproterozoic (835–720 Ma) serpentinites in the Eastern Desert, Egypt: fragments of forearc mantle.* . Geology 2007. **115,** : p. 457–472.
18. El Bahariya GA, A.S., *Petrology and origin of Pan-African serpentinites with particular reference to chromian spinel compositions, Eastern Desert, Egypt: implication for supra-subduction zone ophiolite.* . Third International Conference on the Geology of Africa, Assiut University, Egypt, , 2003: p. 371–388.
19. Zimmer, M., Kröner, A., Jochum, K.P., Reischmann, T., Todt, W., , *The Gabal Gerf complex: a Precambrian N-MORB ophiolite in the Nubian Shield, NE Africa.* . Chemical Geology 1995. **123,** : p. 29–51.
20. Kröner, A., *Ophiolites and the evolution of tectonic boundaries in the late Proterozoic Arabian–Nubian Shield of northeast Africa and Arabia.* . Precambrian Research 1985. . **27,** : p. 277–300.
21. Bakor, A.R., Gass, I.G., Neary, C.R., , *Jabal al Wask, northwest Saudi Arabia: an Eocambrian back-arc ophiolite.* . Earth and Planetary Science Letters 1976. . **30,** : p. 1–9.
22. Abd El-Rahman, Y., Polat, A., Dilek, Y., Fryer, B.J., El-Sharkawy, M., Sakran, S., , *Geochemistry and tectonic evolution of the Neoproterozoic incipient arc–forearc crust in the Fawakhir area, Central Eastern Desert of Egypt.* . Precambrian Research 2009. . **175,** (116–134.).
23. Abdelsalam, M. and R. Stern, *Sutures and shear zones in the Arabian-Nubian Shield.* Journal of African Earth Sciences, 1996. **23**(3): p. 289-310.
24. R.M., S., *Review of late proterozoic sutures, ophiolitic mélanges and tectonics of eastern Egypt and northeast Sudan.* . Geol Rundsch 1994. **83**: p. 537–546.
25. Azer, M.K., *Evolution and economic significance of listwaenites associated with Neoproterozoic ophiolites in south Eastern Desert, Egypt.* Geologica Acta, 2013. **11**(1): p. 113-128.
26. Fitches, W.R., Graham, R.H., Hussein, I.M., Ries, A.C., Shackleton, R.M. and Price, R.C., , *The Late Proterozoic ophiolite of Sol Hamed, NE Sudan.* . Precambrian Res,, 1983. **19:**: p. 385--411.
27. Frey FA, S.J., Stockman HW *The Ronda high temperature peridotite: geochemistry and petrogenesis.* . Geochim Cosmochim Acta 1985. **49:**: p. 2469–2491.

28. Parkinson IJ, P.J., *Peridotites from the Izu–Bonin–Mariana fore-arc (ODP Leg125): evidence for mantle melting and meltmantle interaction in a supra-subduction zone setting.* J Petrol 1998. **39**: p. 1577–1618.
29. Bonatti E, M.P., *Mantle peridotites from continental rifts to oceanic basins to subduction zones. .* Earth Planet Sci Lett., 1989. **9**(297–311).
30. Deschamps F, G.S., Godard M, Chauvel C, Andreani M, Hattori K *In situ characterization of serpentinites from forearc mantle wedges: timing of serpentinization and behavior of fluidmobile elements in subduction zones. .* Chem Geol 2010. **269**: p. 262–277.
31. Stern RJ, G.C., *Origin of late Precambrian intrusive carbonates, Eastern Desert of Egypt and Sudan: C, O, and Sr isotopic evidence. .* Precambr Res 1990 **46**: p. 259–272.
32. Coleman, R.G., *Ophiolites. "Mir", .* 1978. : p. 261 p.
33. Abdel-Karim AM, A.Z., *Possible origin of the ophiolites of Eastern Desert of Egypt, from geochemical prospectives. .* Arab J Sci Eng 2010. **34**: p. 1–27.
34. PA, F., *Oceanic basalts. Blachie and Son Ltd, New York.* 1991
35. Bodinier JL, G.M., *Orogenic, ophiolitic, and abyssal peridotites. In: Carlson RW (ed), Treatise on geochemistry mantle and core: treatise on geochemistry, 2 edn. .* Elsevier Science Ltd, Amsterdam, , 2003: p. pp 103–170.
36. Azer MK, K.A., *Petrological and mineralogical studies of Pan-African serpentinites at Bir Al-Edeid area, central Eastern Desert, Egypt. .* J Afr Earth Sci 2005. **43**: p. 525–536.
37. Jensen, L.S., *A new cation plot for classifying sub-alkaline volcanic rocks. Ontario Division Mines Miscellaneous* 1976. : p. Paper No. 66.
38. Ishii T, R.P., Maekawa H, Fiske R *Petrological studies of peridotites from diapiric Serpentinite Seamounts in the Izu- Ogasawara-Mariana forearc, leg 125. In: Pearce J, Stokking LB, et al (eds), Proceedings of the Ocean Drilling Project, Leg 125, .* Scientific Results (College Station), 1992: p. pp 445–485. .
39. Pearce JA, B.P., Edwards SJ, Parkinson IJ, Leat PT *Geochemistry and tectonic significance of peridotites from the south sandwich arc-basin system, South Atlantic. .* Contrib Miner Petrol 2000. **139**: p. 36–53.

40. Ahmed AH, H.A., *Heterogeneously depleted Precambrian lithosphere deduced from mantle peridotites and associated chromitite deposits of Al'Ays ophiolite, Northwestern Arabian Shield, Saudi Arabia.* . Ore Geol Rev 2015. **67:**: p. 279–296.
41. Hawkins, J.W., *Geology of supra-subduction zones—implications for the origin of ophiolites. In: Dilek, Y., Newcomb, S. (Eds.), Ophiolite Concept and the Evolution of Geological Thought. Boulder, CO,* . Geological Society of America Special 2003. : p. Paper 373, 227–268.
42. Y, N., *Bulk-rock major and trace element compositions of abyssal peridotites: implications for mantle melting melt extraction and post-melting processes beneath mid-ocean ridges.* . J Petrol 2004. **45(12)**: p. 2423–2458.
43. Song, S., Su, L., Niu, Y., Lai, Y., Zhang, L.,, *CH4 inclusions in orogenic harzburgite: evidence for reduced slab fluids and implication for redox melting in mantle wedge.* . Geochimica et Cosmochimica Acta 2009. . **73 (6),**: p. 1737–1754.
44. Godard, M., Lagabrielle, Y., Alard, O., Harvey, J., , *Geochemistry of the highly depleted peridotites drilled at ODP Sites 1272 and 1274 (Fifteen-Twenty Fracture Zone, Mid-Atlantic Ridge): implications for mantle dynamics beneath a slow spreading ridge.* Earth and Planetary Science Letters 2008. . **267**: p. 410–425.
45. Deschamps F, G.M., Guillot S, Hattori K *Geochemistry of subduction zone serpentinites: a review.* . Lithos 2013. **178**: p. 96–127.
46. El-Sayed MM, F.H., Mohamed FH *Geochemical constraints on the tectonomagmatic evolution of the late Precambrian Fawakhir ophiolite, central Eastern Desert, Egypt.* J Afr Earth Sci 1999. **29:**: p. 515–533.
47. ES, F., *Chrome spinels in serpentinites and talc carbonates of the El-Ideid–El Sodmein District, central Eastern Desert, Egypt: their metamorphism and petrogenetic implications.* Chem Erde 2008. **68(2)**: p. 195–205.
48. Khedr MZ, A.S., *Origin of Neoproterozoic ophiolitic peridotites in south Eastern Desert, Egypt, constrained from primary mantle mineral chemistry.* . Mineral Petrol 2013. **107(5)**: p. 807–828.
49. Boskabadi A, P.I., Broman C, Boyce A, Teagle DAH, Cooper MJ, Azer MK, Stern RJ, Mohamed FH, Majka J *Carbonate alteration of ophiolitic rocks in the Arabian-Nubian Shield of*

*Preprints* (www.preprints.org) | NOT PEER-REVIEWED | Posted: 8 October 2019 doi:10.20944/preprints201910.0079.v1



*Egypt: sources and compositions of the carbonating fluid and implications for the formation of Au deposits.* Int Geol Rev 2017. **59(4)**: p. 391–419.

50. Ghoneim MF, S.I., Hamdy MM *Origin of magnesite veins in serpentinites from Mount El-Rubshi and Mount El-Maiyit, Eastern Desert, Egypt. .* Arch Mineral 2003. **54**: p. 41–63.
51. Hamdy MM, L.E., *Metamorphism of ultramafic rocks at Gebel Arais and Gebel Malo Grim, Eastern Desert, Egypt: mineralogical and O-H stable isotopic constraints.* Egypt J Geol 2007. **51**: p. 105–124.
52. C, M., *Serpentinization of abyssal peridotites at mid-ocean ridges. .* C R Geosci, 2003. **335**: p. 825–852.
53. Paulick H, B.W., Godard M, De Hoog JCM, Suhr G, Harvey J *Geochemistry of abyssal peridotites (Mid-Atlantic Ridge, 15°20′N, ODP Leg 209): implications for fluid/rock interaction in slow spreading environments.* Chem Geol 2006. **234**: p. 179–210.
54. Chalot-Prat F, G.J., Lombard A *No significant element transfer from the oceanic plate to the mantle wedge during subduction and exhumation of the Tethys lithosphere (Western Alps).* Lithos 2003. **69:**: p. 69–103.
55. Hattori KH, G.S., *geochemical character of serpentinites associated with high- to ultrahigh-pressure metamorphic rocks in the Alps, Cuba, and the Himalayas: recycling of elements in subduction zones.* Geochem Geophys Geosyst. , 2007.
56. Nockolds, S.R., *The relation between chemical composition and paragenesis in the biotites of micas of igneous rocks.* Am J Sci 1947. . **245(5)**: p. 401–420.
57. Wood, D.A., *The application of a Th–Hf–Ta diagram to problems of tectonomagmatic classification and to establishing the nature of crustal contamination of basaltic lavas of the British Tertiary Volcanic Province. .* Earth Planet Sci. , 1980. . **Lett 50**: p. 11–30.
58. Pearce, J.A., Lippard, S.J., Roberts, S., , *Characteristics and tectonic significance of supra-subduction ophiolites. In: Kokelaar, B.P., Howells, M.F. (Eds.), .* Geological Society of London, Special Publication 1984. . **16,** : p. 777–794.
59. KI, K., *Chromite mineralization in ultramafic rocks of the Wadi Ghadir area, Eastern Desert, Egypt: mineralogical, microchemical and genetic study.* Neues Jb Mineral Abh 2007. **183**: p. 283–296.

Preprints (www.preprints.org) | NOT PEER-REVIEWED | Posted: 8 October 2019 doi:10.20944/preprints201910.0079.v1



60. Geng, H.Y., Sun, M., Yuan, C., Zhao, G.C., Xiao, W.J., , *Geochemical and geochronological study of early carboniferous volcanic rocks from the West Junggar: Petrogenesis and tectonic implications.* Journal of Asian Earth Sciences, 2011. . **v. 42,**: p. p. 854 – 866. .

61. Flower, M.F.J., and Levine, H.M., , *Petrogenesis of a tholeiite–boninite sequence from Ayios Mamas, Troodos ophiolite: evidence for splitting of a volcanic arc* Contribution to Mineralogy and Petrology 1987. **97,** : p. 509– 524.

62. Shervais, J.W., *Ti –V plots and the petrogenesis of modern and ophiolitic lavas.* . Earth Planetary Science Letters 1982. . **59,** : p. 101 –118.

63. DS, O.H., *Serpentinites, records of tectonic and petrological history.* . Oxford Monographs on Geology and Geophysics 1996(no 34.).

64. Snow JE, D.H., *Pervasive magnesium loss by marine weathering of peridotite.* . Geochim Cosmochim Acta 1995 **59:**: p. 4219–4235.

65. Salters VJM, S.A., *Composition of the depleted mantle.* . Geochem Geophys Geosyst. , 2004.

66. Kusky, T.M., and Ramadan, T. M., , *Structural controls on Neoproterozoic mineralization in the South Eastern Desert, Egypt: an integrated field, Landsat TM, and SIR-C/X SAR approach.* Journal of African Earth Sciences,, 2002, . **v. 35, no. 1,** : p. p. 107-121.

67. Ren, D., and Abdelsalam, M. G., , *Tracing along-strike structural continuity in the Neoproterozoic Allaqi-Heiani Suture, southern Egypt using principal component analysis (PCA), fast Fourier transform (FFT), and redundant wavelet transform (RWT) of ASTER data.* Journal of African Earth Sciences, , 2006, . **v. 44, no. 2,** : p. p. 181-195.

68. Abdeen, M.M., and Abdelghaffar, A. A., , *Syn-and post-accretionary structures in the Neoproterozoic Central Allaqi-Heiani suture zone, Southeastern Egypt.* Precambrian Research, , 2011, . **v. 185, no. 3-4,** : p. p. 95-108.

69. Ibrahim, W., Watanabe, K., Ibrahim, M., and Yonezu, K.,, *Neoproterozoic Tectonic Evolution of Gabal Abu Houdied Area, South Eastern Desert, Egypt: As a Part of Arabian–Nubian Shield Tectonics.* Arabian Journal for Science and Engineering,, 2015, . **v. 40, no. 7,** : p. p. 1947-1966.

70. Pohl, W., *Genesis of magnesite deposits—models and trends.* Geologische Rundschau, 1990. **79**(2): p. 291-299.

 doi:10.20944/preprints201910.0079.v1




71. Allegre CJ, P.J., Humler E, Hofmann AW *The chemical composition of the Earth.* . Earth Planet. Sci. Lett., 1995. **134**: p. 515-526.
72. Arif M, M.C., *Goechemistry of serpentinized peridotites from the Indus Suture Ophiolite in Swat, NW Pakistan.* Geol. Bull. Univ. Peshawar 2003. **36:** : p. 1-10.
73. Dardir, A.A., Elshimi, K.A.M., , *Geology and geochemical exploration for gold in the banded iron formation of Um Nar area, Central Eastern Desert, Egypt.* . Ann. Geol. Surv. Egypt 1992. . **18**,: p. 381– 409.
74. Takla, M.A., Suror, A.A.,, *On the occurrence of Ni-sulphides and arsenides in some Egyptian serpentinites.* . Egypt. Mineral. , 1996. **8**: p. 1 –18.
75. Botros, N.S., *Geological and geochemical studies on some gold occurrences in the north Eastern Desert, Egypt.* . PhD thesis, Zagazig Univ., Zagazig, Egypt. , 1991: p. 146 pp.
76. Oweiss, K.A., El Naggar, A.A., Abdel Razik, K.A., Moselhy, N., Ali, A.B., , *Gold exploration at the Heianai area, South Eastern Desert, Egypt.* . Ann. Geol. Surv. Egypt 2001. . **24,** : p. 435–450.
77. Ramadan, T.M., Ibrahim, T.M., Said, A.D., Baiumi, M., , Application of remote sensing in exploration for uranium mineralization in Gabal El Sela area, south Eastern Desert, Egypt. . The Egyptian Journal of Remote Sensing and Space Science 2013. . 16, : p. 199-210.
78. McDonough, W.F., Sun, S-s., The composition of the Earth. . Chemical Geology 1995. 120,: p. 223-253.
79. Jagoutz E, P.H., Baddenhausen H, Blum K, Cendales M, Dreibus G, Spettel B, Lorenz V, Wanke H The abundances of major, minor and trace elements in the earth's mantle as derived from primitive ultramafic nodules. . Proc. Lunar Planet. Conf. 10:, (1979) p. 2031-2050.
80. Hart SR, Z.A., In search of a bulk-Earth composition. Chem Geol 1986. 57:: p. 247-267.
81. Gokhale, N.W., Chemical composition of biotite as a guide to ascertain the origin of granites. . Bull Soc Geol 1968. Fin 40: p. 107–111.
82. Streckeisen, A., Classification of common igneous rocks by mean of their chemical composition. A provisional attempt. . Neues Jahrbuch für Mineralogie – Abhandlungen 1976. : p. 1–15.
83. Pohl, W., Genesis of magnesite deposits—models and trends. Geologische Rundschau,, 1990, . v. 79, no. 2, : p. p. 291-299.